BIROn - Birkbeck Institutional Research Online

Quaternary uplift of palaeoshorelines in southwestern Crete: the combined effect of extensional and compressional faulting

J. Robertson [a,*], G.P. Roberts [a], A. Ganas [b], M. Meschis [c], D.M. Gheorghiu [d], R.P. Shanks [d]

[a] School of Natural Sciences, Birkbeck College, University of London, WC1E 7HX, UK
[b] Institute of Geodynamics, National Observatory of Athens, Athens, Greece
[c] Institute Nazionale di Geofisica e Vulcanologica (INGV), Palermo, Italy
[d] Scottish Universities Environmental Research Centre (SUERC), East Kilbride, UK

ARTICLE INFO

ABSTRACT

We undertake spatio-temporal analysis on sequences of Pleistocene palaeoshorelines in southwestern Crete where deformed Holocene marine notches have predominantly been suggested to be linked to coseismic uplift from the 365 CE Mw > 8 earthquake. Previous investigations into the Holocene notches have been used to infer that the dominant mechanism of uplift may be slip either on a reverse crustal fault or on the subduction interface. However, seismic reflection studies attest to the presence of numerous active offshore extensional faults whose role in the long-term deformation is unclear. The relative contributions of upper-plate extensional and compressional faults to the overall deformation can be assessed through the study of uplifted and deformed Late Quaternary palaeoshorelines. New ^{36}Cl exposure dating on wave-cut platforms and palaeoshoreline mapping are combined with existing age controls to facilitate investigation into the deformed Late Quaternary palaeoshorelines. We observe that the Late Quaternary uplift rates increase from west (0.61 mm/yr) to east (0.83 mm/yr) over ~20 km, a spatial uplift pattern that is inconsistent with published vertical deformation models of slip solely on the subduction interface or on a reverse crustal fault. Elastic half-space modelling suggests that an offshore extensional fault may also contribute to the uplift. We conclude that a combination of active extensional and compressional faults may be responsible for Late Quaternary uplift across southwestern Crete.

1. Introduction

Southwestern Crete displays evidence of sustained uplift during the Late Quaternary in the form of raised Holocene marine palaeoshorelines and sequences of Late Quaternary palaeoshorelines that have been used to investigate the potential faults responsible for the deformation (e.g., Pirazzoli et al., 1996; Shaw et al., 2008; Ganas and Parsons, 2009; Stiros, 2010; Tiberti et al., 2014; Mouslopoulou et al., 2015a, 2015b; Ott et al., 2019; Ott et al., 2021). Such indirect observations on faults are important because they improve our ability to undertake fault-based seismic hazard assessment in areas where faults are difficult to directly observe and have recurrence intervals that exceed the ~100-year instrumental records. Presently, at least four hypotheses have been invoked to explain the deformation in southwestern Crete: (i) slip on offshore normal faults (Ott et al., 2021), (ii) slip on the subduction interface (Pirazzoli et al., 1996; Papadimitriou and Karakostas, 2008), (iii) slip on a reverse crustal

fault that may splay from the subduction interface (Stiros and Drakos, 2006; Shaw et al., 2008, 2010; Stiros, 2010; Mouslopoulou et al., 2015b) (Fig. 1) and (iv) focusing on plate interface and upper-plate fault slip because of the 3D-funnel shape of the subduction geometry (Ganas and Parsons, 2009). This paper attempts to differentiate between the causal uplift scenarios by providing additional constraints on the uplift from new dating and mapping of deformed Pleistocene palaeoshorelines on the southwestern coast of Crete.

Previous studies investigating the uplift of southwestern Crete have predominantly focused on a prominent marine notch suggested to have experienced up to ~9 m of coseismic uplift in the corner of southwestern Crete near to Elafonissi (Fig. 2) decreasing in elevation along the coastlines north and east of Elafonissi, during the 365 CE (Common Era) Mw > 8 earthquake (Pirazzoli et al., 1996; Stiros, 1996; Shaw et al., 2008, 2010; Stiros and Drakos, 2006; Tiberti et al., 2014; Mouslopoulou et al., 2015b). This putative megathrust earthquake has been linked,

using historical reports, to strong ground motions and a tsunami that caused wide-spread destruction throughout the eastern Mediterranean. Specifically, the near-total destruction of >100 towns in Crete and collapsed houses and ruined towns as far away as Cyprus and along coasts of Libya and Alexandria have been documented (Stiros, 2001; Ambraseys, 2009; Papadopoulos, 2011). Radiocarbon dating on marine

fossils removed from within the 9 m notch combined with historical records have been employed to associate uplift of the notch with the 365 CE earthquake (e.g., Pirazzoli et al., 1996; Shaw et al., 2008, 2010; Stiros, 2010; Mouslopoulou et al., 2015a). The significant coseismic uplift that the above authors have associated with the 365 CE event has been linked with slip on a reverse fault because it is suggestive of a large
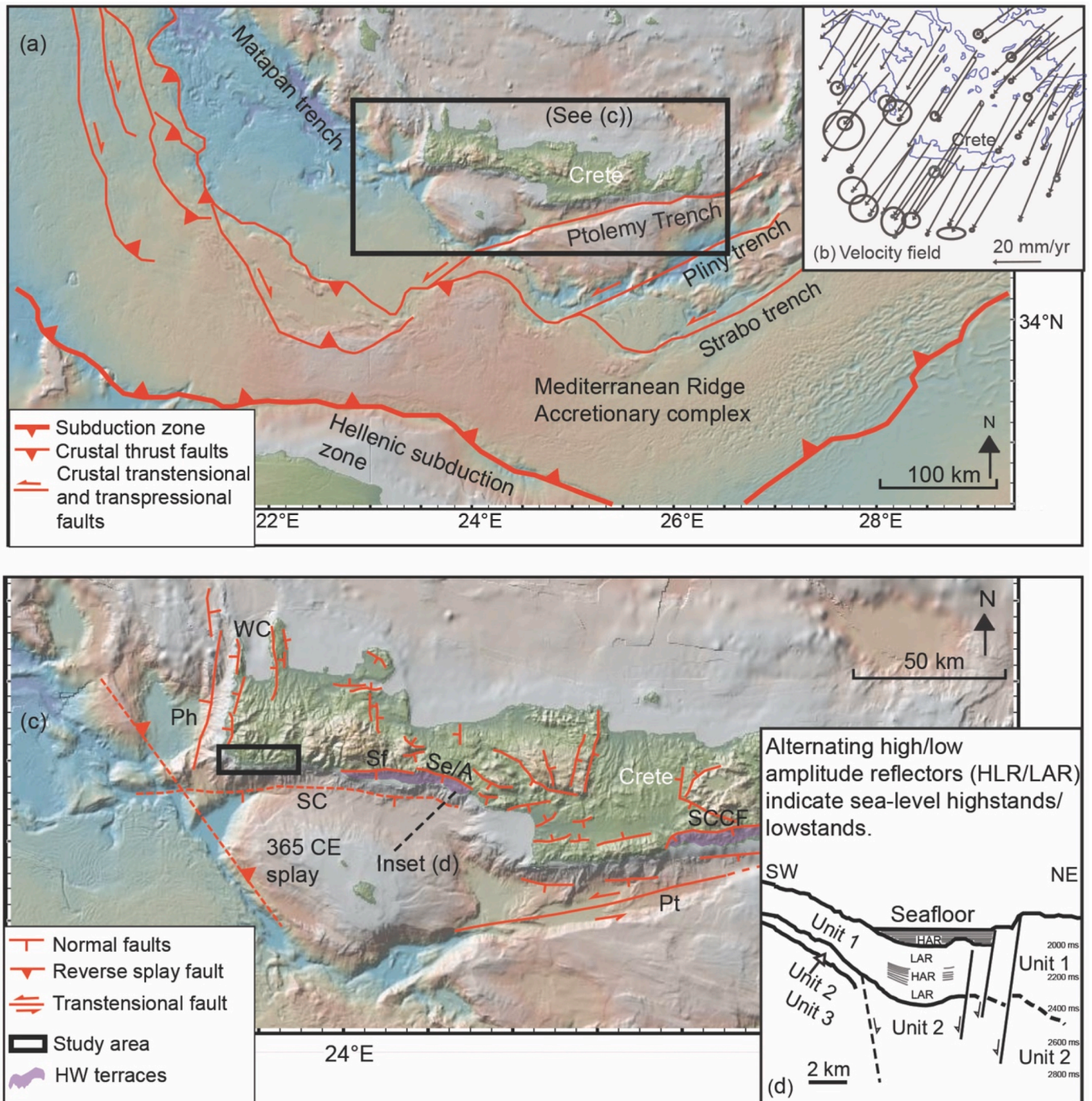

Fig. 1. (a) Tectonic setting of Crete, Greece. The location of the Hellenic Subduction Zone and crustal faults within the Hellenic Subduction Zone are taken from Kreemer and Chamot-Rooke (2004). (b) Simplified velocity field for Greece (using Nocquet, 2012). (c) Map of Crete and simplified upper crustal fault map (Robertson et al., 2019; Nicol et al., 2020), Ph: Phalasarna fault, WC: Western Crete fault; Pt: Ptolemy fault. Dashed faults are postulated and discussed herein. SC marks the maximum extent of the fault trace for the South Crete fault discussed herein. The 365 CE splay is the proposed location of a crustal reverse splay fault from Shaw et al. (2008). Also shown are the locations of uplifted hangingwall marine terraces for the south coast of Crete associated with the following faults: Sfakia (Sf); Sellia/Asomato (Se/A) and South Central Crete (SCCF) fault (Tsimi et al., 2007; Robertson et al., 2019). (d) Line drawing (see (c) for location) of a seismic profile from Alves et al. (2007) (their Fig. 4a) illustrating units 1–3 offset by normal faults identified in seismic sections alongside alternating high and low amplitude reflections (HAR and LAR) suggested to be associated with sea-level highstands and lowstands, respectively.

rupture area, and thus earthquake magnitude (e.g., Stiros and Drakos, 2006; Papadimitriou and Karakostas, 2008; Shaw et al., 2008, 2010; Stiros and Drakos, 2006; Tiberti et al., 2014; Mouslopoulou et al., 2015b). Elastic dislocation modelling and analysis of instrumental era fault plane solutions combined with the notch radiocarbon ages lead Shaw et al. (2008) to invoke a reverse crustal fault that splays from the subduction interface as the causative 365 CE fault. However, the magnitude of coseismic uplift associated with this potential tsunami-genic earthquake and its causal fault mechanism continue to be debated (e.g., Ganas and Parsons, 2009; Ott et al., 2021). Ott et al. (2021) obtained new radiocarbon fossil ages from the deformed notch that they used with existing notch radiocarbon ages to investigate the age spread of the data against known earthquakes between 3000 and 1000 years Cal BP. These authors identified that "… several historical events fall into the range of the observed emergence ages" and used this evidence to

suggest that uplift of the southwestern coastline of Crete may have occurred in multiple earthquakes preceding the 365 CE event, casting doubt on the uplift of the 9 m notch in a single event. An alternative explanation invoked by Ott et al. (2021) to explain the uplifted notch and the 365 CE associated tsunami is clustered earthquakes on N–S and E-W trending normal faults located offshore Crete (Fig. 1c, faults 'Ph' and 'SC'). Ganas and Parsons (2009) questioned the presence of the postulated splay fault from Shaw et al. (2008) based on the absence of microseismicity 20–40 km beneath western Crete, instead suggesting that the 365 CE earthquake occurred on the subduction interface. Ganas and Parsons (2009) used a 3D finite element model of the Hellenic arc to model a Mw > 8 event on the subduction interface offshore Crete. These authors showed that such an earthquake is not capable of producing coseismic uplift greater than 2.5 m and, as such, their findings do not support only the 365 CE scenario to explain the uplifted notch. Theories

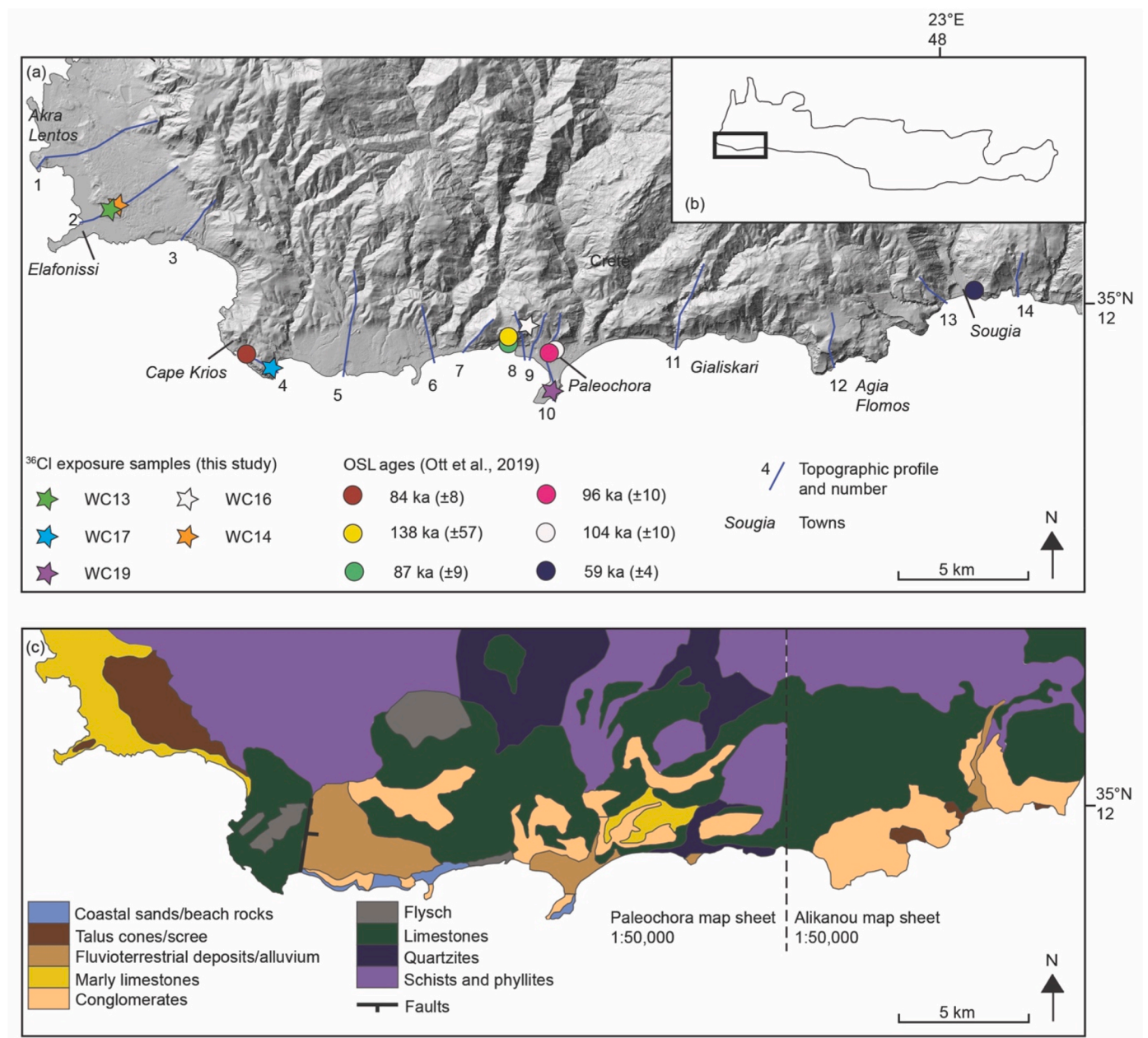Fig. 2. (a) DEM of the study area (see (b)), locations of topographic profiles are shown alongside the new [36]Cl exposure dating locations and existing OSL ages from Ott et al. (2019). (c) Simplified geological map of the study area using map sheets (1:50,000) Paleochora and Alikanou (Institute for Geology and Mineral Exploration (IGME), 1969, Institute for Geology and Mineral Exploration (IGME), 1995).

surrounding the causal fault associated with the 365 CE earthquake are pertinent to investigating Pleistocene uplift in southwestern Crete because it has been inferred that the cause of short-term (Holocene) deformation may also be responsible for deformation over longer timescales. For example, Mouslopoulou et al. (2015b) use palaeoshoreline elevation observations and age controls from the southern coastline of Crete alongside numerical modelling to suggest that uplift along the Cretan Hellenic margin over 50 kyrs is predominantly achieved by earthquakes on large crustal reverse faults. The finding from Mouslopoulou et al. (2015b) contrasts with other studies on Late Pleistocene palaeoshorelines along the Cretan Hellenic margin that document palaeoshoreline deformation associated with multiple onshore and offshore extensional faults over the past ~900 kyrs (e.g., Tsimi et al., 2007; Gaki-Papanastassiou et al., 2009; Gallen et al., 2014; Robertson et al., 2019).

Pleistocene palaeoshorelines provide a record of coastal deformation over hundreds of thousands of years and analysis of the spatial pattern of uplift rates obtained from sequences of palaeoshorelines can yield insight into the cause of the deformation. Palaeoshorelines represent geomorphological markers in the landscape formed during sea-level highstands associated with interglacial periods (Alexander, 1953; Lajoie, 1986). Coastlines hosting sequences of palaeoshorelines afford excellent opportunities to investigate long term tectonic deformation because evidence of fault motion can be inferred from spatial and temporal uplift rate variation (e.g., Muhs et al., 1992; Berryman, 1993; Westaway, 1993; Armijo et al., 1996; Roberts et al., 2009; Saillard et al., 2009, 2011; Roberts et al., 2013; Binnie et al., 2016; Meschis et al., 2018; Robertson et al., 2019, 2020; Ferranti et al., 2021). Specifically, if the deformation of palaeoshorelines is to be attributed to faulting, then it is expected that the length scale of deformation and spatial patterns of uplift should be concordant with the expected displacement patterns of the dominant fault in question (e.g., Armijo et al., 1996; Roberts et al., 2009; Howell et al., 2017; Litchfield et al., 2020; Robertson et al., 2019). In other words, displacement gradients on faults that have produced the uplift should produce uplift gradients over the same length-scale and position. Thus, investigations of deformed palaeoshorelines provide insight into the possible causes of observed deformation because they constrain the uplift rates and allow inverse modelling of the slip-rates on active faults in the region; such rates are essential for seismic hazard assessment.

The sequence of Late Pleistocene palaeoshorelines visible in southwestern Crete have been explored in previous studies (Wegmann, 2008; Strasser et al., 2011; Tiberti et al., 2014; Mouslopoulou et al., 2015a; Ott et al., 2019). However, the robustness of the conclusions from some of these studies is debated (Ott et al., 2019). This means that the pattern of Pleistocene uplift within southwestern Crete is not constrained well enough to allow comparisons between the spatial patterns of long-term uplift versus Holocene uplift obtained from the notches. Determining the uplift rates of palaeoshorelines is reliant on constraining the age of at least one palaeoshoreline within a sequence in order that undated palaeoshorelines can be correlated with sea-level highstands (Burbank and Anderson, 2013). Previous studies along southwestern Crete have used palaeoshorelines to propose uplift rates that vary temporally and spatially between −3.2 and 7.7 mm/yr (Wegmann, 2008; Shaw et al., 2008; Strasser et al., 2011; Tiberti et al., 2014; Mouslopoulou et al., 2015a; Ott et al., 2019). In more detail, along the 30 km section of coastline from Elafonissi to Sougia (Fig. 2), the studies of Wegmann (2008), Shaw et al. (2008), Tiberti et al. (2014) and Mouslopoulou et al. (2015a) employed radiocarbon dating on fossils to date Late Pleistocene palaeoshorelines up to ~55 m above sea level. The age results from these studies imply high uplift rates that, in some cases, indicate significant temporal variability over the past 50 kyrs (2 mm/yr (Shaw et al., 2008), 0–7 mm/yr (Mouslopoulou et al., 2015a), −2.6–3.2 – 7.7 mm/yr (Tiberti et al., 2014) and 1.1–1.8 mm/yr (Wegmann, 2008)). Furthermore, the radiocarbon ages from uplifted Pleistocene palaeoshorelines were used by Mouslopoulou et al. (2015a) to imply that palaeoshorelines can form

throughout the sea-level cycle and survive passage through the wave zone multiple times, a concept that deviates from accepted models of palaeoshoreline formation during interglacial highstands (Lajoie, 1986). A study by Busschers et al. (2014) suggests that Late Pleistocene radiocarbon ages on marine molluscs are complex to interpret and may represent minimum ages. Busschers et al. (2014) presented radiocarbon ages of 30–50 ^{14}C ky BP on mollusc shells that were significantly younger than the MIS 5 (>75 ka) ages indicated by biostratigraphy, U–Th dating, OSL dating and age-depth relationships with sea level. These authors speculated that younger carbon contamination within the shells may be responsible for the age discrepancy. A study carried out by Ott et al. (2019) compared new and existing Pleistocene radiocarbon ages from fossils along western Crete to OSL ages from the same locations. Their results reinforced those of Busschers et al. (2014), observing that at sites where multiple radiocarbon ages were obtained, the ages were inconsistent and that in comparison to the OSL ages, the radiocarbon ages were significantly younger. Ott et al. (2019) questioned whether published Pleistocene radiocarbon ages older than ~30 ka (e.g., Wegmann, 2008; Shaw et al., 2008; Tiberti et al., 2014; Mouslopoulou et al., 2015a) can reliably be used for Pleistocene palaeoshoreline age and uplift rate determinations on western Crete.

Existing OSL palaeoshoreline age controls suggest that the southwest of Crete has been uplifting at rates between 0.5 and 1.1 mm/yr since the mid-late Pleistocene (Ott et al., 2019). We aim to further refine these uplift rates and investigate long-term faulting using palaeoshoreline elevation measurements from field studies and high-resolution satellite-derived digital elevation models (DEM), alongside ^{36}Cl exposure dating on erosional wave-cut platforms augmented with the existing OSL ages (Ott et al., 2019). In-situ ^{36}Cl within carbonate surface rocks predominantly forms when the earth's surface is exposed to the atmosphere. ^{36}Cl exposure dating can be used to directly constrain the formation ages of Pleistocene carbonate erosional wave-cut platforms and has yielded age determinations on wave-cut platforms elsewhere on Crete and on the Perachora Peninsula (Greece) that agree with existing independent age controls (Robertson et al., 2019, 2020). The palaeoshoreline age and elevation data within this study facilitates interrogation of spatial uplift rate changes along a ~30 km section of the coastline that encompasses the uplifted 365 CE notch sites along the southwest coast of Crete. We find that (i) the uplift rates increase from 0.61 (±0.12) mm/yr in the western extent to 0.83 (±0.14) mm/yr 20 km to the east after which they appear to decrease, and (ii) that these uplift rates have been temporally constant since ~400 ka. Comparisons between the spatial Late Quaternary uplift rate pattern and those from coseismic vertical deformation models (obtained from the literature and from elastic half-space modelling carried out herein) using published reverse and extensional fault traces reveal that the Late Quaternary spatial uplift rate pattern is not compatible with uplift dominated solely by slip on a reverse crustal or the subduction megathrust. We suggest that the Late Quaternary spatial pattern of uplift may be explained if the effect of offshore extensional faults is included. The implications of our findings are briefly discussed relative to the potential seismic hazard of southwestern Crete and the dynamics of the upper plates of subduction systems.

2. Background

Crete is in the forearc of the 1200 km long Hellenic subduction zone, where convergence between the Eurasian and African plates occurs at a rate of 35–40 mm/yr (Nocquet, 2012) and is dominated by the relative southward motion of the Eurasian plate (Jackson, 1994) (Fig. 1). Ongoing forearc extension since the mid Miocene (e.g., Fassoulas et al., 1994; Ten Veen and Meijer, 1998; Alves et al., 2007) results in a complex tectonic regime onshore and offshore Crete. Offshore, a combination of subduction-related convergence occurs at depths below ~15 km whilst extensional/transtensional faulting dominates above ~15 km (Papazachos, 1990; Papazachos et al., 2000; Ten Veen and Kleinspehn, 2003;

Meier et al., 2004; Alves et al., 2007; Tsimi et al., 2007; Kokinou et al., 2012; Sakellariou and Tsampouraki-Kraounaki, 2019). Onshore, arc normal and arc parallel extension dominates (Mercier et al., 1989; Taymaz et al., 1990; Armijo et al., 1992; Ten Veen and Meijer, 1998; Ten Veen and Kleinspehn, 2003; Caputo et al., 2010; Zygouri et al., 2016; Ganas et al., 2017) (Fig. 1c) evidenced by E-W, NE-SW and NW-SE trending faults that have been active throughout the Holocene and the Late Pleistocene (e.g., Armijo et al., 1992; Caputo et al., 2010; Ott et al., 2019; Robertson et al., 2019; Nicol et al., 2020; Mechernich et al., 2022; Ganas et al., 2022). In places along the eastern, southern, and western Cretan coastlines, extensional faults that strike parallel to the coastlines downthrow marine terraces in their hangingwalls (Skourtsos et al., 2007; Tsimi et al., 2007; Gaki Papanastassiou et al., 2009; Caputo et al., 2010; Ott et al., 2019; Robertson et al., 2019, Fig. 1c). The local fault related hangingwall subsidence produced by the onshore faults has been suggested to be counteracted by uplift from a combination of footwall uplift from offshore faults, possibly in addition to a broader regional uplift signal associated with sediment underplating (Gallen et al., 2014; Ott et al., 2019, 2021; Robertson et al., 2019).

Seismic reflection studies indicate numerous extensional/transtensional faults are located offshore southern Crete (e.g., Mascle et al., 1982; Kreemer and Chamot-Rooke, 2004; Meier et al., 2004; Alves et al., 2007; Kokinou et al., 2012; Sakellariou and Tsampouraki-Kraounaki, 2019) (e.g., Fig. 1d). Within these studies, there is general agreement that an offshore south dipping, E-W trending extensional fault bounds the southwest coastline, coinciding with a ~3 km deep bathymetric trough (Fig. 1c) (see also EMODnet Bathymetry https://www.emodnet-bathymetry.eu). However, the exact location and length of the fault(s), and indeed whether there is one continuous offshore fault or multiple faults along strike is not agreed upon.

Variable lithology is present in southwestern Crete because of Oligocene to Miocene south-directed thrusting (Fassoulas et al., 1994, and references therein; Papanikolaou and Vassilakis, 2010) (Fig. 2c). Triassic to Cretaceous limestones dominate, with areas of Pliocene marly limestones, and Pleistocene fluvio-terrestrial deposits and coastal beach rocks/sands (Institute for Geology and Mineral Exploration (IGME), 1969, Institute for Geology and Mineral Exploration (IGME), 1995 map sheets Alikanou 1:50,000; Paleochora 1:50,000). Sequences of palaeoshorelines, identified as palaeo-sea-cliffs and their associated erosional wave-cut platforms or marine terraces, provide evidence of sustained uplift throughout the Late Quaternary (Angelier, 1979; Pirazzoli et al., 1982; Shaw et al., 2008; Tiberti et al., 2014; Mouslopoulou et al., 2015a; Ott et al., 2019). In combination with the timing and elevations of sea-level highstands from sea-level curves (e.g., Siddall et al., 2003) and present-day palaeoshoreline elevations (orthometric heights), age constraints on palaeoshorelines can be used to allocate undated palaeoshorelines to sea-level highstands and investigate long-term uplift rates (e.g., Westaway, 1993; Armijo et al., 1996; Houghton et al., 2003; Roberts et al., 2009; Saillard et al., 2011; Roberts et al., 2013; Jara-Munoz et al., 2015; Meschis et al., 2018; Pedoja et al., 2018; Normand et al., 2019; Robertson et al., 2019).

A palaeoshoreline is a relict shoreline represented by the intersection between an erosional wave-cut platform, or marine terrace, and sea cliff (Lajoie, 1986). Erosional wave-cut platforms form coevally with their up-dip palaeoshorelines during highstands, when sea level is relatively stable, as a result of wave action and mass wasting that exposes new rock in the shallow marine environment that is then further exposed above sea level (Alexander, 1953; Lajoie, 1986; Bradley and Griggs, 1976; Muhs et al., 1994; Anderson et al., 1999; Trenhaile, 2000) (Fig. 3). Exposure of new rock on a carbonate platform to the atmosphere results in ^{36}Cl accumulation. Therefore, platforms that have not been significantly eroded since formation or experienced post-formation sedimentary cover may be excellent candidates for in-situ ^{36}Cl cosmogenic exposure dating to constrain the sea-level highstand responsible for the formation of the platform (e.g., Stone et al., 1996; Robertson et al., 2019, 2020; Choi and Seong, 2021). Cosmogenic exposure dating relies on
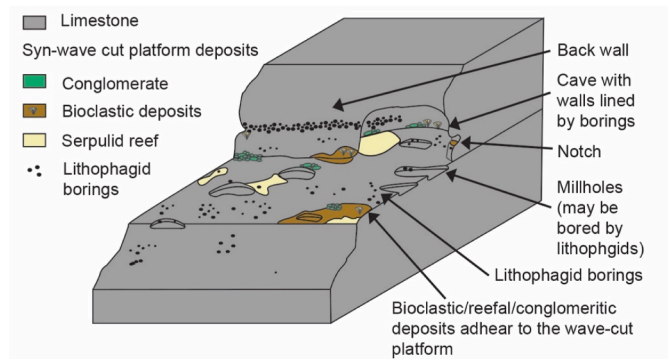

Fig. 3. Schematic diagram of the features expected on an erosional wave-cut platform, where preserved lithophagid borings and millholes indicate that erosion rates are low enough to allow for ^{36}Cl exposure dating (modified from Robertson et al., 2019).

knowledge of the behaviour of cosmic rays that undergo reactions as they enter the Earth's atmosphere prior to impinging on the Earth's surface (Dunai, 2010). The abundance of cosmogenic isotopes in a given rock sample can be used alongside the production rate of the cosmogenic isotopes to obtain an exposure age for the sample given information on, amongst other things, the rock chemistry and surface erosion rates (e.g., Phillips et al., 2001; Schimmelpfennig et al., 2009; Dunai, 2010; Marrero et al., 2016b). One of the first documented applications of ^{36}Cl to date a wave-cut platform (formed during the Holocene) was carried out by Stone et al. (1996), which inspired the approach of Robertson et al. (2019, 2020) to constrain the ages of Pleistocene palaeoshorelines in south central Crete and the Gulf of Corinth, Greece, respectively. The reliability of ^{36}Cl exposure dating on wave-cut platforms was reinforced in the studies of Robertson et al. (2019, 2020) who obtained ^{36}Cl exposure ages that agreed with age results from other independent dating methods (U–Th on corals and OSL on sediments) associated with the same palaeoshorelines. Robertson et al. (2019, 2020) emphasise the importance of sampling for ^{36}Cl exposure dating on platforms where there is evidence of minimal erosion since platform exposure above sea level in the form of preserved lithophagid borings and millholes (Fig. 4; Section 3.2).

3. Methods

This research examines the spatial uplift pattern of southwestern Crete's Pleistocene palaeoshorelines to explore potential causal faults responsible for the uplift. Key to fulfilling this aim is the identification and measurement of palaeoshoreline elevations, absolute dating of wave-cut platforms and uplift modelling to correlate palaeoshoreline elevations with sea-level highstands and, elastic half-space deformation modelling to investigate possible offshore causal faults. Our approach is outlined below in more detail.

3.1. Palaeoshoreline elevations

Palaeoshoreline elevations were collected from a combined approach using a 5-m DEM (error of ±4 m) (produced by Ktimatologio SA from air-photo stereopairs) (Fig. 2a) and from field studies during 2018. The palaeoshorelines were initially identified on the DEM from 14 serial 2D topographic profiles (referred to as P1-14; Fig. 2a) where a break of slope, the inflection points between what were assumed to be sub-horizontal wave-cut platforms and vertical to sub-vertical palaeo sea-cliffs, was taken as the elevation of the palaeoshoreline. Palaeoshorelines observed on the DEM were subsequently investigated in Google Earth to check that the breaks of slope were not associated with "human-made" features and on geological maps to ensure they did not represent lithological changes or faults. Where possible,

palaeoshorelines were verified and investigated in greater detail during a field campaign in 2018. Note that because this study focuses on Pleistocene uplift rates, we do not document observations on the ~9 m notch associated with Holocene coseismic uplift (Pirazzoli et al., 1996; Shaw et al., 2008, 2010; Stiros, 2010; Mouslopoulou et al., 2015a; Ott et al., 2021).

Palaeoshorelines were identified in the field using geomorphic features associated with the physical process of shoreline formation and evidence of from organisms that are known to live in shallow marine environments. Geomorphic evidence is represented by a palaeo-sea-cliff that may host a cave and/or notch (a groove formed in the palaeo-sea-cliff), in addition to the presence of an erosional wave-cut platform located a few decimetres to meters down dip of the palaeoshoreline (e.g. Pirazzoli, 1986; Ferranti et al., 2006; Roberts et al., 2013; Antonioli et al., 2015; Rovere et al., 2016; Robertson et al., 2019) (Fig. 4). Where a notch was observed, field-based palaeoshoreline elevations were measured from the middle of the vertical extent of the notch using a hand-held barometric altimeter (error of ±3 m) that was regularly recalibrated to sea level. In the absence of a notch the elevations were obtained from the intersection between the wave-cut platform and the palaeo-sea-cliff or cave wall (as per Pirazzoli, 2005). Erosional wave-cut platforms may host millholes, circular depressions formed by the action of pebbles scouring the surface because of wave agitation, and partial veneers of cemented beach deposits predominantly composed of rounded to sub-rounded pebbles and cobbles (e.g., Laborel and Laborel-Deguen, 1994; Miller and Mason, 1994; Roberts et al., 2009; Bird, 2011; Robertson et al., 2019, 2020). In addition to being associated with sub-horizontal wave-cut surfaces, palaeoshorelines may also be located updip from upstanding pinnacles that are typically a few decimeters high (e.g., Robertson et al., 2019). Where the tops of upstanding pinnacles are at the same elevation (±~5 cm), it can generally be accepted that they represent a palaeo-wave-cut surface. We also sought evidence of shallow marine organisms that are known to adhere to wave-cut surfaces, notches and palaeo-cliffs such as vermetid and serpulid reefs, coralline algae, and borings from sponges and the mollusc Lithophaga (Stephenson and Stephenson, 1949; Laborel, 1986; Laborel and Laborel-Deguen, 1994; Rovere et al., 2016).

3.2. ^{36}Cl exposure dating: sampling and age determinations

When a newly formed carbonate wave-cut platform is exposed to the earth's atmosphere, ^{36}Cl will begin to accumulate. Measurements of the concentration of ^{36}Cl from a wave-cut platform sample and knowledge of the expected production rates of ^{36}Cl at a given location on earth can be used to determine the exposure age of the sampled wave-cut platform. Studies of ^{36}Cl cosmogenic production rates show that: (i) ^{36}Cl production decreases exponentially with depth and, (ii) that the dominant production pathway changes from spallation in the upper 2 m of the surface to slow negative muon capture below 2 m (Gosse and Phillips, 2001; Heisinger et al., 2002a, 2002b; Licciardi et al., 2008; Schlagenhauf et al., 2010). Consequently, if significant erosion since initial platform exposure is not recognised when sampling, the production rate used to calculate the exposure age may be incorrect. For example, the production rate 1 m below the surface may be ~50% of the value at the original surface (Schlagenhauf et al., 2010). In response to this, we placed importance on sampling from locations where indicators of low erosion since platform formation are present (as per the approach in Robertson et al., 2019, 2020). We aim to sample from wave cut platforms that exhibit lithophagid borings and/or millholes. Specifically, we remove samples from the wave-cut surface that contain vertically bored lithophagid borings and/or are located on the outer edge of millholes because their presence suggests that erosion cannot exceed the depth of the original dimensions of the preserved feature since the formation of the wave-cut platform. We consider the samples removed from upstanding pinnacles with horizontal borings into the tops or sides of the pinnacles as speculative sites because it is possible that the rock above

the horizontal borings may have been subjected to unknown erosion. We think it is worth sampling the speculative sites and are confident in the approach we use to assess the reliability of the ^{36}Cl age determinations (outlined below). It is also important to carry out detailed mapping such that sample sites have not experienced sedimentary cover since wave-cut platform formation because an exposure-cover-re-exposure history may result in an erroneous exposure age (e.g., Robertson et al., 2019).

Within this study ^{36}Cl exposure samples were removed from wave-cut surfaces using a hammer and chisel noting the sample elevation, Universal Transverse Mercator (UTM) coordinates, altitude, latitude, and topographic shielding measurements. Documenting the latitude and altitude of sample sites are important because ^{36}Cl production rates vary depending where on the earth the samples are removed from, for instance, higher production rates occur at higher altitudes and latitudes. Analysis of topographic shielding on the sample sites is made to ascertain the exposure of the sample site to a full hemisphere of open sky (Balco et al., 2008). Measurements of inclination (in degrees) between the sample site and open sky were made every 30° for a full 360° and the shielding value calculated using trigonomic functions in a shielding calculator (Tibor Dunai, Pers. Comms. 2016). The shielding value is used as an input in the exposure age modelling so that the production rate at each sample site takes into account the topography surrounding the sample. Preparation of the samples initially involved washing them in distilled water in an ultrasonic bath and allowing them to air dry. They were then crushed to a 'gravel sized' fraction using a jaw crusher and subsequently milled to a 125–250 μm fraction using a disc mill; both the jaw crusher and disc mill were thoroughly cleaned between the processing of each sample.

The ^{36}Cl sample preparation method and production of targets from crushed fractions prior to accelerator mass spectrometry was completed as per the method outlined by Schimmelpfennig et al. (2009) at the Scottish Universities Environmental Research Centre (SUERC). Sample data were obtained from accelerator mass spectrometry (AMS) and analysis using inductively coupled plasma optical emission spectrometry (ICP-OES) (also carried out at SUERC). Each sample output dataset reports the concentration of ^{36}Cl atoms per gram of sample, the bulk rock weight of key oxides (e.g., CaO and NaO) and chemical elements, and the analytical uncertainties associated with all reported values. The data for each sample was used in combination with its field-based measurements and associated uncertainties (longitude, latitude, elevation, topographic shielding, erosion rate) alongside the selected production rate scaling model ('Sa' used herein as per Marrero et al., 2016b) to create an input file (Supplementary Table 1) used in the CRONUScalc programme (www.cronus.cosmogenicnuclides.rocks/2.0/). CRONUScalc is an online tool used to calculate the exposure age of each sample using known production pathways and the data from each sample's input file (Marrero et al., 2016b).

The erosion rate used within the input file is particularly important because, as explored above, inaccurate values have the capacity to result in erroneous exposure ages (Marrero et al., 2016a, 2016b). Field observations on lithophagid borings are used to inform the erosion rates applied herein, based on knowledge that the average depth of lithophagid borings is ~6 cm (Devescovi and Iveša, 2008). Lithophagid borings at the sample locations indicate total erosion of approximately 2–4 cm since palaeoshoreline formation, which equates to erosion rates of 0.16–0.32 mm/ky over 125 ka and 0.26–0.56 mm/ky over 76 ka. Selecting the exact erosion rate for each site is challenging because we do not know the initial depth of the borings. Herein, exposure ages are calculated using 0.2 mm/ky as a minimum value. However, we recognise that there is uncertainty associated with the erosion rate and undertake sensitivity tests calculating the exposure ages using 0.4, 0.6 and 0.8 mm/ky to check the effect that the range of possible erosion rates has on the exposure ages (Section 4.2). The limit of 0.8 mm/ky was selected because at rates above this, we expect that the preserved lithophagid borings would have been completely eroded (assuming the average

lithophagid boring depth at formation of 6 cm). Our sensitivity tests reveal that the ^{36}Cl ages plot in the same sea-level highstands when erosion rates between 0.2 and 0.8 mm/ky are used in the age determinations.

The output of CRONUScalc is an exposure age with internal and external uncertainties, where internal uncertainties are linked to the analytical uncertainties associated with the AMS and the external uncertainties are a representation of the propagated production-rate and measured uncertainties combined with the analytical uncertainty. Marrero et al. (2016b) notes that the internal uncertainties alone may underestimate the realistic uncertainties, and as such, external uncertainty values should be reported. We assess reliability of ^{36}Cl age determinations for each sample using: (i) analysis of the concentrations of ^{36}Cl atoms per gram of rock relative to the elevation of the sample, because Robertson et al. (2019) showed that sequences of ^{36}Cl exposure dated palaeoshorelines displayed higher ^{36}Cl concentrations with increasing elevations, (ii) evidence of low erosion since platform formation, and (iii) knowledge of the timing of sea-level highstands, because reliable exposure age determinations for palaeoshorelines should be close to the timing of known sea-level highstands.

3.3. Existing age controls

Age controls from palaeoshorelines on southwestern Crete from the study of are used herein to complement new ^{36}Cl exposure ages and inform our uplift modelling. We opt not to use existing radiocarbon ages on Pleistocene palaeoshorelines in the study area because of the challenges associated with interpreting the reliability of radiocarbon ages on marine fossils >30 ka, as outlined in the Introduction. The OSL Pleistocene age determinations from within the study area (Fig. 2; Ott et al., 2019) appear to agree with the timings of known sea-level highstands. Within this study, we compare our exposure dating results to the OSL ages (Ott et al., 2019) and use the OSL ages in addition to our ^{36}Cl exposure ages to calculate uplift rates on topographic profiles.

3.4. Correlating palaeoshorelines with sea-level highstands

Derivation of uplift rates from sequences of palaeoshorelines requires the correlation of sea-level highstands to dated and undated palaeoshorelines. Herein, we apply the synchronous correlation approach (developed by Houghton et al., 2003 and applied in Roberts et al., 2009, 2013; Meschis et al., 2018; Pedoja et al., 2018; Robertson et al., 2019; De Santis et al., 2021; Meschis et al., 2022). This method of correlation is designed to make use of the fact that Quaternary sea-level highstands are unevenly spaced in time and hence if uplift rates are constant through time the elevation unevenness of the palaeoshorelines will mirror the highstand elevation unevenness. Specifically, this method allows an entire sequence of palaeoshorelines to be allocated to sea-level highstands in a synchronous manner as opposed to sequentially matching a palaeoshoreline to a sea-level highstand one at a time. The synchronous correlation method also considers that at uplift rates below ~1 mm/yr younger sea-level highstands may overprint and erode older palaeoshorelines (e.g., Robertson et al., 2019; De Santis et al., 2023). Synchronous correlation is facilitated using the 'Terrace Calculator' (Houghton et al., 2003) which is populated by sea-level curve data (Siddall et al., 2003) detailing the age of each sea-level highstand and the elevation of the sea-level at that time (relative to the present-day sea level). The calculator allows investigation of changes in uplift rates as different uplift-rate values can be assigned to particular time periods by the user, but investigation initially tests the simplest hypothesis of a constant uplift-rate, only preceding to time-varying uplift-rates if a match with measured palaeoshoreline elevations cannot be achieved.

For each topographic profile (Fig. 2), the uplift rate (u) is determined through iteration until the predicted elevation of a highstand within the Terrace Calculator matches the measured elevation of a dated palaeoshoreline. In turn this results in calculation (Eq. (1)) of the predicted

elevations (E_{pred}) of all highstands along the topographic profile in question using the age of the highstands (T) and the sea level elevations (SL) of the highstands relative to today's sea level (Eq. (1)) (Robertson et al., 2019). The measured palaeoshoreline elevations are matched against the predicted palaeoshoreline elevations if they agree with one another within ± 10 m. The goodness of fit between the predicted and measured palaeoshoreline elevations for each profile was evaluated using linear regression (R^2). This approach results in an uplift rate per topographic profile. To ensure that each uplift rate is as representative as possible, we attempt to minimise the Root Mean Square Error (RMSE) by iterating the uplift from 0.1 to 1.0 mm/yr at intervals of 0.05 mm/yr; the uplift rate result with the lowest RMSE is applied to the topographic profile (see Fig. 4 in Robertson et al., 2019 for a graphical explanation of this process).

$$E_{Pred} = (T \times u) + SL \tag{Eq. 1}$$

To accompany each uplift rate, all uncertainties were propagated using the equation for standard error (SE) (Eq. (2)), where u is the uplift rate, σH is the combined uncertainty for measured palaeoshoreline elevation and sea level relative to today, HT is the measured palaeoshoreline elevation, HSL is the sea level for the highstand in question, and T is the highstand age related to the terrace formation. This revealed propagated uncertainties in the region of 0.09–0.16 mm/yr.

$$SE\,(u)^2 = u^2\left(\left(\frac{\sigma_{H^2}}{\left(H_T - H_{SL}\right)^2}\right) + \left(\frac{\sigma_{T^2}}{T^2}\right)\right) \tag{Eq. 2}$$

For topographic profiles that do not have age controls from ^{36}Cl exposure dating or OSL dating, we laterally mapped palaeoshorelines along strike in the DEM and/or during fieldwork. Where a dated palaeoshoreline intersected with another topographic profile this provided an age control for the neighbouring profile and allowed the approach described above to be applied. We have five topographic profiles that have an absolute age constraint in the form of an OSL (Ott et al., 2019) or ^{36}Cl exposure age. From P1 (Akra Lentos) to 10 (Gialiskari) and at P14 (Sougia) (Fig. 2) it was possible to use either absolute age controls on a topographic profile or a mapped dated palaeoshoreline to calculate the uplift rate. From P11 (Akra Flomos) to 13 (Sougia) (Fig. 2), tracing the palaeoshorelines is judged less reliable owing to steep and variable lithology (Fig. 2c, Institute for Geology and Mineral Exploration, 1969 map sheet, Alikianou 1:50,000). In this instance, an alternative method was employed (from Robertson et al., 2019) that involved using the measured palaeoshoreline elevations to test all uplift scenarios for a topographic profile by, in turn, allocating the lowest measured palaeoshoreline to each highstand on the calculator, applying the resultant uplift rate to the topographic profile and matching the measured palaeoshorelines to the predicted palaeoshorelines. For each attempt, the number of matches between measured and predicted palaeoshorelines, the R^2 and the RMSE were used to identify the best fit uplift rate.

Pleistocene sea-level data forms a critical component within our uplift rate calculations (see Eq. (1)). Comparisons of data from different sea-level curves have revealed highstand age and elevation variations such that caution should be applied when making uplift assumptions based upon the data from a single curve. This is because sea-level elevations from different sea-level curves can yield varying results regarding the allocation of palaeoshorelines to highstands, which may in turn affect calculated uplift rates (Caputo, 2007). Robertson et al. (2019) acknowledged this challenge when investigating Late Quaternary palaeoshoreline uplift associated with the South-Central Crete Fault. Like the present study, Robertson et al. (2019) allocated undated palaeoshorelines to highstands using the Terrace Calculator, populated with sea-level curve data from Siddall et al. (2003). However, they tested the reliability of their uplift observations by also modelling uplift rates using data from four additional sea-level curves (Lambeck and Chappell, 2001; Waelbroeck et al., 2002; Shakun et al., 2015; Spratt and

Lisiecki, 2016). Whilst small variations in the highstand to palaeo-shoreline allocations were observed when differing sea-level curves were employed, a key finding was that an almost identical spatial variation of uplift rates was observed. Thus, we are confident that modelling the uplift using a single sea-level curve should not bias the overall spatial results.

3.5. Pleistocene and coseismic uplift patterns to investigate causal faults

Comparison between the Late Quaternary spatial uplift rate pattern and coseismic uplift patterns on fault traces in southwest Crete are used to provide insight into the possible causal fault(s) associated with the Late Quaternary deformation. This is because coseismic vertical deformation modelling can be used as a proxy for the expected pattern of long-term vertical deformation (e.g., Robertson et al., 2019). In this study we assume that the fault(s) in question rupture along their full-length during earthquakes. We construct along-strike highstand elevation and uplift rate plots (following the approach in Section 3.4) to examine the spatial change in uplift rates throughout the Late Quaternary taking into account the presence of minor faults suggested by Ott et al. (2019) to strike normally to the coastline (Fig. 2c). Our Late Quaternary spatial uplift rate pattern is compared to modelled coseismic vertical deformation data for slip on: (i) a reverse crustal splay fault as described by Shaw et al. (2008), (ii) the subduction interface as described by Ganas and Parsons (2009), and (iii) extensional faults from Mascle et al. (1982), Kreemer and Chamot-Rooke (2004), Alves et al. (2007), Kokinou et al. (2012), and Sakellariou and Tsampouraki-Kraounaki (2019). Coseismic uplift on the extensional faults is modelled herein from elastic-half space modelling using the Matlab code of Mildon et al. (2016) combined with Coulomb 3.4 software (Toda et al., 2011). In this approach, fault data (trace, rake, dip, dip direction) is used in the code of Mildon et al. (2016) to create a rupture along the extensional fault in question. The subsurface slip for each fault is iterated within the code until the earthquake magnitude from rupturing the fault matches the maximum earthquake magnitude calculated using total fault-length scaling relationships (from Wells and Coppersmith (1994)). The output fault slip distribution data is then used to model the coseismic vertical deformation in Coulomb 3.4 (Toda et al., 2011), the results of which are displayed as 2D vertical contours of uplift and subsidence. We overlay the image of the 2D vertical contours from Coulomb onto Google Earth to identify the coseismic uplift values at each topographic profile. The coseismic uplift at each topographic profile for all fault traces are then presented against the distance along strike.

4. Results

This section presents the field observations and palaeoshoreline elevations obtained during fieldwork and analysis of the DEM (Fig. 4). Age constraints from new [36]Cl exposure ages and existing age controls are presented (Figs. 5 and 6) and used in uplift modelling to allocate dated and undated palaeoshorelines to sea-level highstands (Fig. 7). Uplift rates from individual profiles are then examined to constrain the spatial uplift rate pattern (Fig. 8). We then model the coseismic vertical deformation obtained from slip on offshore extensional faults (Fig. 9).

4.1. Field mapping and palaeoshoreline elevations

Field observations reveal sub horizontal surfaces comprised of Neogene marly limestones, Cretaceous basement limestones, Cretaceous flysch and Pleistocene alluvial fan deposits (Fig. 2c). In places throughout the study area these lithologies are unconformably overlain by patches of cemented beach deposits, the tops of which reveal planed-off surfaces (Fig. 4). The beach deposits include beach sands, bioclastic deposits and marine back-beach cemented conglomerates, the facies of these marine deposits suggests that they represent the upper shoreface

environment, with their planed-off surfaces indicative of erosion from wave action. The sub-horizontal surfaces are predominantly seaward dipping surfaces that host millholes and lithophagid borings, with borings most frequently observed on surfaces comprised of basement limestone, marly limestone, bioclastic deposits and limestone cobbles within marine conglomerates. In places, pinnacles of upstanding limestone that host lithophagid borings and stand a few decimeters high are visible on the observed surfaces. Where upstanding pinnacles are visible, we note that the tops of the pinnacles are at similar heights (± 5 cm) suggesting that they may collectively define a palaeo-surface. We interpret the sub-horizontal surfaces and those that display upstanding pinnacles as wave-cut platforms and the bioclastic deposits, sands and conglomerates as syn-wave cut platform deposits. The wave-cut platforms throughout the research area intersect up dip with sub-vertical back walls, notches and/or sea caves that have been bored by lithophagids and are interpreted as palaeoshorelines (e.g., Fig. 3). The following paragraphs describe examples of palaeoshorelines defined by the break of slope between palaeo-sea-cliffs up-dip from wave-cut platforms and detail palaeoshoreline elevation measurements. Some variation in along strike palaeoshoreline elevations for the same shoreline is expected if the uplift is fault related and because of stated uncertainties on the DEM.

Field observations and DEM measurements in the area of Elafonisi (P1, P2 and P3, Fig. 4a–f, Table 1) reveal a relatively low-lying peninsula. A platform at ~22 m comprised of marly limestone hosts preserved millholes, lithophagid borings, patches of bioclastic deposits and planed off wave-cut pebbles cemented onto the platform surface (Fig. 4a–c). The lithophagid borings on the 22 m marly limestone platform made it an excellent candidate for [36]Cl exposure dating (Sample WC13) (Fig. 4c). The 22 m wave-cut platform terminates up dip against a palaeo-sea cliff at 25 m (Fig. 4a) which is laterally continuous in the field and DEM northwest of P1 to southeast of P3 for ~500 m. The platform sequentially higher than the 25 m palaeoshoreline is at 30 m, with its palaeo-sea-cliff at 40 m (Fig. 4d, Table 1). Toward the seaward edge of the 30 m platform there are a few upstanding pinnacles of basement limestone that are in places draped by patches of bioclastic packstone containing angular basement limestone clasts (Fig. 4e and f). Lithophagid borings are apparent on the sides of the pinnacles and the angular clasts of basement limestone within the packstone show evidence of sponge borings (Fig. 4f). We sampled the bored bioclastic packstone from one of the pinnacles for [36]Cl exposure dating (WC14).

Southeast of P3, a stepped profile is visible in the landscape on the headland of Cape Krios (P4; Figs. 2 and 4g, Table 1). The basement limestone that forms the Cape hosts multiple seaward sloping surfaces that have been bored by lithophagids and contain millholes close to the palaeo-sea-cliffs and toward the seaward edge of the surfaces. Rocky palaeo-sea-cliffs on Cape Krios are visible at elevations of 12, 17, 29, 42 and 91 m (Table 1) and display small caves, notches and localised lithophagid borings leading us to interpret Cape Krios (P4) as a sequence of palaeoshorelines (Fig. 4g). Downdip from the 91 m palaeoshoreline are pinnacles of upstanding basement limestone with small patches of bioclastic beach sands attached. Lithophagid borings are visible in the sides of the basement limestone pinnacles. At the 75 m seaward edge of the platform associated with the 91 m palaeoshoreline we observed localised areas of planed-off, lithophagid bored limestone surfaces indicative of a preserved wave-cut platform. We sampled for [36]Cl exposure dating from the limestone wave-cut surface at 75 m where a vertically bored lithophagid boring provided confidence that erosion since platform formation would be acceptably low (WC17) (Fig. 4i).

P5 and P6 are within a bay where the lithology up to ~80 m is dominated by a Pleistocene alluvial fan above which the higher, incised, topography of Cretaceous-Eocene limestones occurs (Institute for Geology and Mineral Exploration, 1995 map sheet Paleochora 1:50,000, Fig. 2c). Agricultural greenhouses have been built on the alluvial fan surface and field evidence of palaeoshorelines and wave-cut platforms is difficult to observe. The DEM profiles reveal breaks of slope on P5 at 52,
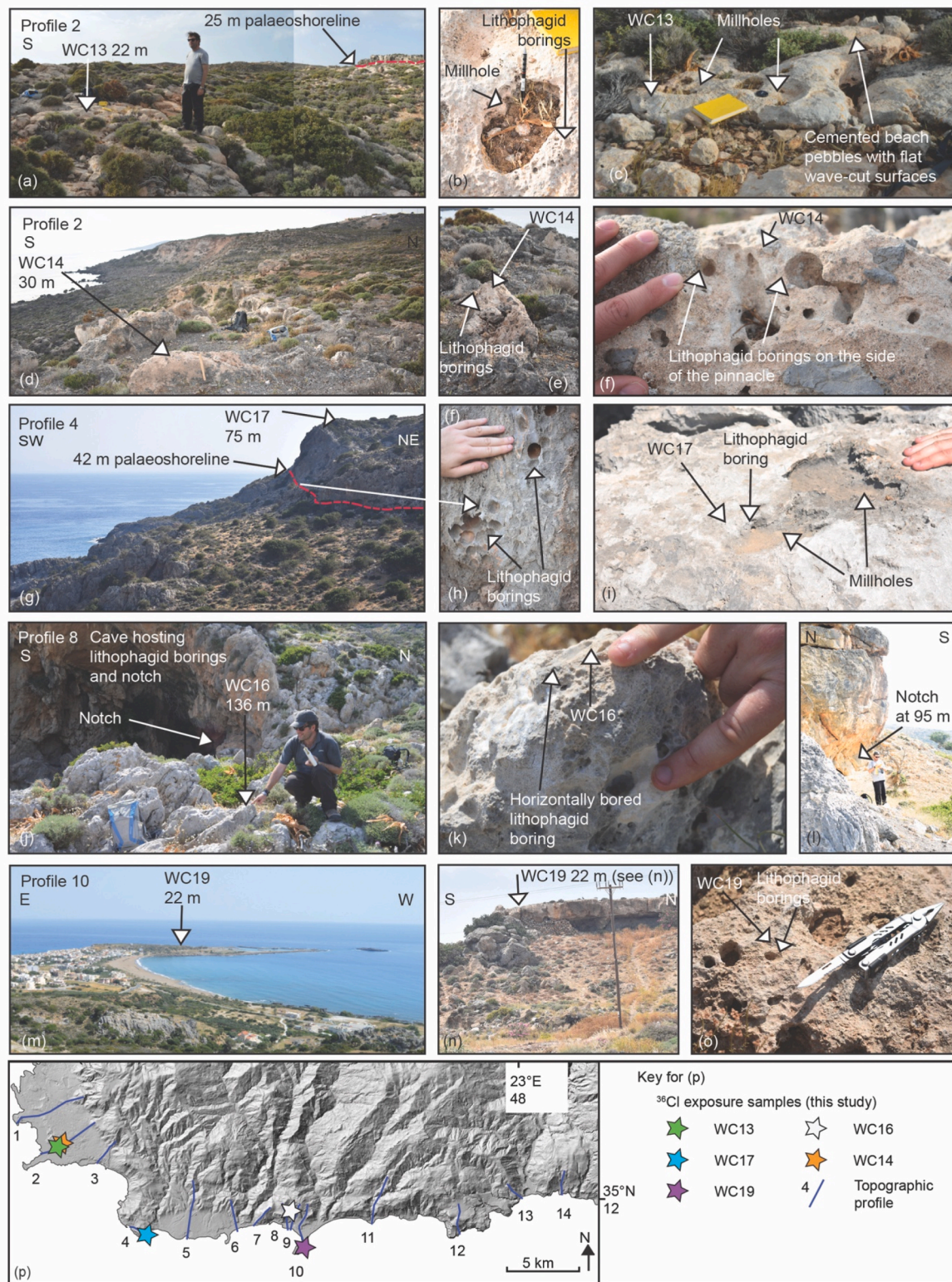
Fig. 4. [36]Cl exposure sampling locations on wave-cut platforms for WC13 (a–c), WC14 (d–f), WC17 (g–i), WC16 (j, k, l) and WC19 (m, n, o) showing evidence of low erosion indicators in the form of lithophagid borings and millholes, see (p) for the locations of the topographic profiles and [36]Cl sample locations in this study. See Table 2 for [36]Cl data for all samples and Supplementary Table 1 for all input data used in CRONUScalc for age determinations.

100, 144, 266 m and on P6 at 33, 53, and 148 m (Table 1). The breaks of slope observed on the two profiles do not appear to be associated with human-made features and show broadly similar elevations, suggesting that they may represent laterally continuous palaeoshorelines.

A sequence of palaeo-sea-cliffs is visible throughout the Paleochora

area (P7–P10) in the field and on the DEM topographic profiles (Fig. 4, Table 1). Field observations were made on P8. We observe notches hosting lithophagid borings at 12 and 18 m. At 52 m lithophagid borings occur on a palaeo-sea-cliff located 5 m along strike from a small cave at 54 m. Located on the seaward dipping surface associated with the 54 m

palaeoshoreline is a ~1 m high cemented beach conglomerate composed of rounded pebbles and cobbles. Above the 54 m palaeoshoreline on P8, a notch and lithophagid borings are visible on the palaeo-sea-cliff at 95 m (Fig. 4l). However, immediately down-dip from the 95 m palaeoshoreline the surface dips steeply seaward and wave-cut platform evidence is lacking. At ~140 m on P8 a cave and notch (Fig. 4j) with lithophagid borings on the roof of the notch represent palaeoshoreline evidence. Adjacent to the cave, lithophagid borings are visible on the bedrock limestone pinnacles. We sampled one of these pinnacles for ^{36}Cl exposure dating (WC16) (Figs. 2 and 4k), removing the top of the pinnacle and a horizontally bored lithophagid boring.

Within the Paleochora area a promontory is located along P10 (Figs. 2 and 4m). The surface of the promontory is a horizontal platform at 22 m composed of a ~1 m thick marine deposit that unconformably overlies basement limestone. Below the 22 m platform we observe a notch cut into the both the limestone and marine deposits at 16 m (Figs. 2, 4n and Table 1). In more detail, rounded limestone pebbles and cobbles occur at the base of the marine deposits, above which are marine sands containing disarticulated oyster shells that are in turn overlain by a bioclastic algal serpulid reef. Bioclastic packstone deposits are visible toward the outer edge of the platform surface. We interpret this sequence as marine terrace deposits. In places, the marine terrace surface and deposits, the basement limestone, and the limestone cobbles and pebbles have been intensely bored by lithophagids. We also note the presence of millholes around the seaward edge of the platform suggesting the surface of the marine terrace is a wave-cut platform. We sampled for ^{36}Cl exposure dating from a lithophagid bored bioclastic packstone surface at 22 m close to the edge of the wave-cut platform (Fig. 4o). Landward from the 22 m wave-cut platform, the topography decreases to 5–10 m above sea level before rising again to reveal a sequence of palaeoshorelines at 34, 58, 95 and 211 m (Table 1). It is not clear from the field/DEM observations if the palaeoshoreline associated with the 22 m wave cut platform has been eroded or if it belongs to the 34 m palaeoshoreline, we suspect based on the horizontal distance

between the 22 m platform and the 34 m palaeoshoreline that a palaeoshoreline may be missing.

The rocky coastline east of Paleochora (P11, Fig. 2) is composed of Mesozoic limestones. Close to Sougia (P13-14, Fig. 2), Miocene conglomerates are the dominant lithology (Fig. 2c, Institute for Geology and Mineral Exploration, 1969 map sheet, Alikianou 1:50,000). Except for the Sougia area (P14) where we observe a notch at 12 m, the palaeoshorelines from P11 to P14 are typically very steep and physically inaccessible so we use the DEM to investigate break of slope elevations and Google Earth to ensure these are not 'Human made'. We observe some consistency between the elevations of palaeoshorelines along the 10 km between P11-14 (Table 1) which gives us confidence in the measurements: (i) palaeoshorelines are observed on P11-14 at 35–40 m, (ii) on P11 and P13 there are palaeoshorelines at 52 and 58 m, respectively, (ii) on P11-14 there are palaeoshorelines between 101 and 109 m and, (iv) P11-14 have palaeoshorelines at 151–161 m.

Several palaeoshorelines investigated herein were also detailed in 2023)Ott et al. (2019. We include palaeoshoreline elevations from Ott et al. (2019, 2023) in Table 1 where they are co-located with our measurements. We note that there is generally good agreement between palaeoshorelines elevations from the DEM and field studies herein and the field studies of Ott et al. (2019, 2023).

4.2. ^{36}Cl exposure ages

Results from the five ^{36}Cl exposure ages sampled from P2, P4, P8 and P10 (Figs. 2 and 4) obtained from CRONUScalc using the input data in Supplementary Table 1 are presented in Fig. 5 and Table 2. The ages presented are determined using erosion rates of 0.2 mm/ky (Section 3.2) with sensitivity tests on age determinations carried out for erosion rates of 0.4, 0.6 and 0.8 mm/ky (Fig. 5c).

Sample WC13 was removed from the 22 m wave-cut platform associated with the 25 m palaeoshoreline along P2 (Figs. 2 and 4). The ^{36}Cl exposure age of this sample was 66.3 (±8.2) ka (Fig. 5, Table 2) which
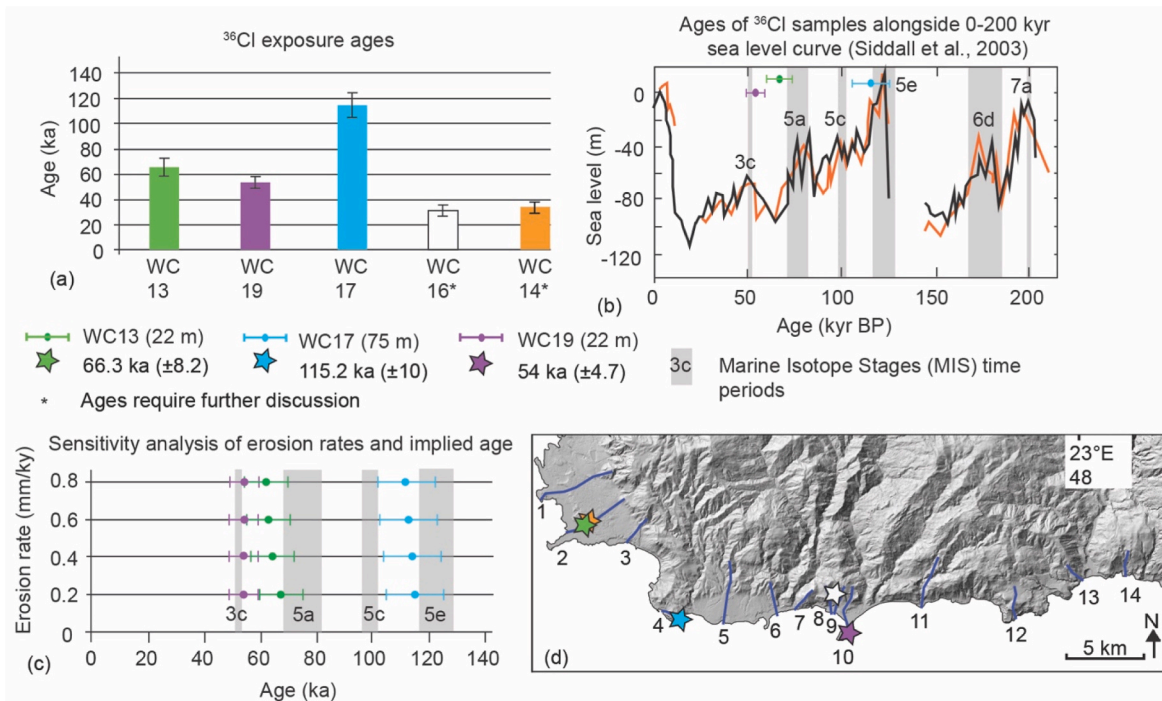
Fig. 5. (a) ^{36}Cl exposure ages for WC13, WC14, WC16, WC17 and WC19, samples WC14 and WC16 are suggested to be eroded ages, see text for discussion. (b) Plots of the ^{36}Cl exposure ages for samples WC13, WC17 and WC19 against the sea-level curve of Siddall et al. (2003) shows that the ages align with sea-level highstands. (c) Sensitivity tests of changing erosion rates in age determinations within CRONUScalc from 0.2 to 0.8 mm/ky to illustrate that higher erosion rates still place the ^{36}Cl exposure ages broadly within the sea-level highstands. Maximum erosion rates of 0.8 mm/ky are suggested owing to the presence of low erosion indicators at the sample sites (see text and Fig. 4). (d) DEM of the study area showing the locations of ^{36}Cl samples.
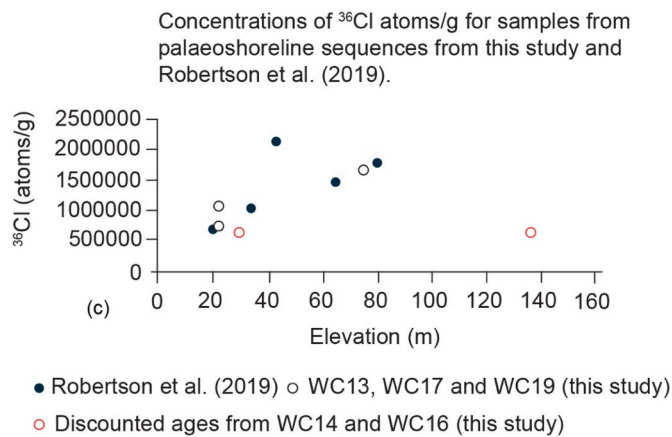
Fig. 6. Plot of ^{36}Cl concentrations against sample elevations for samples dated in this study and from Robertson et al. (2019) to illustrate that the concentration of ^{36}Cl atoms per gram are expected to increase with elevation.

suggests its formation occurred during MIS 5a (~76 ka highstand) (Fig. 5b). Sample WC17, located along P4 was removed from close to the outer edge (75 m) of the 91 m palaeoshoreline (Figs. 2 and 4). It yielded an age of 115.2 ($\pm$9.99) ka. Fig. 5b shows that WC17 can be allocated to the MIS 5e (~125 ka) highstand. Sample WC19 was removed from the surface of the 22 m wave-cut platform on P10 (Figs. 2 and 4). The CRONUScalc age for WC19 is 54 ($\pm$4.7) ka suggesting that the 22 m wave-cut platform may be associated with the ~55 ka highstand of MIS 3c (Fig. 5b).

For completeness, we also present and briefly discuss the ^{36}Cl exposure ages from samples WC14 at 30 m (33.4 $\pm$ 3.4 ka) and WC16 at 136 m (33.1 $\pm$ 3.1 ka) (Figs. 2, 4 and 5; Table 2) that imply association with MIS 3a. We question the reliability of the age determinations of WC14 and WC16 (Section 3.2) because the ^{36}Cl concentration of these samples are significantly lower than other ^{36}Cl exposure samples in this study that have been sampled from lower elevations (Table 2, Fig. 6). Robertson et al. (2019) showed that sequences of ^{36}Cl exposure dated palaeoshorelines displayed increasing concentrations of ^{36}Cl atoms per gram of rock as elevation increases because higher, and therefore older, palaeoshorelines have been exposed for greater periods of time (Fig. 6). Sample WC14 was taken from a pinnacle with lithophagid borings on the sides of the pinnacle (Fig. 4f), whilst sample WC16 was removed from a pinnacle whose top surface displayed a horizontal lithophagid boring (Fig. 4k) (compare these to samples WC13, WC17 and WC19 that were removed from wave cut platforms displaying vertical lithophagid borings (Fig. 4b, i, o, respectively)). We suspect that the tops of the sampled pinnacles of WC14 and WC16 may have experienced higher than acceptable levels of erosion, perhaps because material above the borings has toppled off since wave-cut platform formation. Erosion of surfaces since initial exposure will lower the measured cosmogenic nuclide concentrations in samples because it brings material to the surface that has previously been partially shielded by cosmic rays (Dunai, 2010). Thus, eroded samples will tend toward ages that are erroneously young. Led by our ^{36}Cl concentration analyses and informed by our sampling observations we suggest that the ^{36}Cl exposure ages for WC14 and WC16 are consistent with samples that have experienced higher than acceptable levels of erosion and resulted in erroneously low ^{36}Cl exposure ages. Consequently, we do not consider them further in this study.

The importance of selecting ^{36}Cl exposure samples from locations that appear to have experienced minimal erosion, using preserved features such as millholes, and lithophagid borings that are vertically bored into the wave-cut surface has been emphasised throughout this study and by Robertson et al. (2019, 2020). Samples WC13, WC17 and WC19 were all sampled from surfaces hosting vertically bored lithophagid

borings. The age determinations for these samples are calculated within CRONUScalc using erosion values of 0.2 mm/ky and this equates to total erosion of 15 mm and 25 mm for samples associated with the 76 ka and 125 ka highstands, respectively (Section 3.2). Sensitivity tests that examine the age determination differences using erosion rates of 0.4, 0.6 and 0.8 mm/ky on samples WC13, WC17 and WC19 reveal that adjusting the erosion rates for each sample results in a 0.3%–7% change in ^{36}Cl exposure ages (Fig. 5c). Importantly, for samples WC13, WC17 and WC19, the age determinations obtained using the upper possible erosion rate of 0.8 mm/ky still broadly place the wave-cut platforms within the MIS identified using erosion rates of 0.2 mm/ky.

In summary, we obtain three ^{36}Cl exposure ages from along P2 (WC13), P4 (WC17) and P10 (WC19) that indicate palaeoshoreline formation during known sea-level highstands (Fig. 5). We exclude two age determinations (WC14 and WC16) based upon very low concentrations of ^{36}Cl atoms per gram. Furthermore, we demonstrate that age determinations made using erosion rates between 0.2 and 0.8 mm/ky do not alter the highstand allocations of the sampled palaeoshorelines.

4.3. Correlating palaeoshorelines with sea-level highstands to determine uplift rates

In this section we carry out uplift modelling using the terrace calculator to: (i) compare the ^{36}Cl exposure ages obtained herein to OSL age determinations from Ott et al. (2019) and, (ii) calculate uplift rates for topographic profiles 1–14 using the ^{36}Cl exposure ages and OSL ages from Ott et al. (2019). Palaeoshoreline to sea-level highstand correlations were carried out as per the approach described in Section 3.3. As a brief reminder, palaeoshorelines with age controls, or palaeoshorelines that are traceable along strike from a dated palaeoshoreline, are used to form an initial hypothesis for the uplift rate. Within the terrace calculator, we apply the uplift rate obtained from the dated palaeoshoreline to the entire topographic profile and attempt to match the predicted palaeoshoreline elevations for each sea-level highstand to measured palaeoshoreline elevations from the DEM or fieldwork (provided the predicted palaeoshoreline elevations are within $\pm$10 m of the measured elevation). In other words, the dated palaeoshorelines drive correlation of undated palaeoshorelines with sea-level highstands. The fit between the measured and predicted elevation datasets is evaluated using regression analysis (R^2) (Fig. 7o). We move to a time-varying uplift rate only if an acceptable correlation between measured and predicted palaeoshoreline elevations cannot be achieved using an uplift rate that is constant through the late Quaternary (e.g., Roberts et al., 2009).

We find consistency between most of the ^{36}Cl exposure age controls and the OSL ages from Ott et al. (2019) where the same palaeoshoreline is dated in both studies and when more than one palaeoshoreline on the same (or neighbouring) topographic profiles are dated in both studies. In more detail, there are two ages that can be mapped between the 22–29 m palaeoshoreline visible from P1 to P4 (Fig. 7a–d, Table 3). Ages of 66.3 ($\pm$8.2) ka from WC13 from this study on P2 (Fig. 7b) and the 84 ($\pm$8) ka age from Ott et al. (2019) on P4 (Fig. 7d) indicate palaeoshoreline formation during the 76 ka highstand within MIS 5a (in agreement with the age interpretation from Ott et al. (2019). Uplift modelling using these age controls implies uplift rates of 0.62, 0.64, 0.65 and 0.69 mm/yr from P1 to P4, respectively. Furthermore, on P4 (Fig. 7d, Table 3), in addition to the 26 m palaeoshoreline allocated to MIS 5a by Ott et al. (2019), we use ^{36}Cl exposure dating to associate the 91 m palaeoshoreline with the 125 ka (MIS 5e) highstand (115.2 ka ($\pm$10 ka) Sample WC17). We find that the elevations of the dated MIS 5a and 5e palaeoshorelines on P4 can be replicated through modelling using the uplift rate of 0.69 mm/yr (Fig. 7d, Table 3). We therefore conclude that the OSL and ^{36}Cl exposure ages of WC13 and WC17 are robust and that the resultant uplift rates are reliable.

Within the Paleochora area there are four age controls located between P8 and P10 (Fig. 2). The distance between P8 and P10 is just ~1 km so we undertake uplift modelling collectively on these topographic

profiles to investigate whether the age controls can be explained using the same rate of uplift. We adopt this approach because we expect that over such a short horizontal distance, the uplift rates should not differ by more than a few tenths of a mm (e.g., Roberts et al., 2009, 2013;

Robertson et al., 2019). Ott et al. (2019) obtain an OSL age of 87 (±9) ka (Sample P-916-o-2) (Fig. 2) for the 14 m palaeoshoreline on P8 that they allocate to the 76 ka highstand (MIS 5a) which can be explained using an uplift rate of 0.5 mm/yr. On the 56 and 58 m palaeoshorelines on P8 and
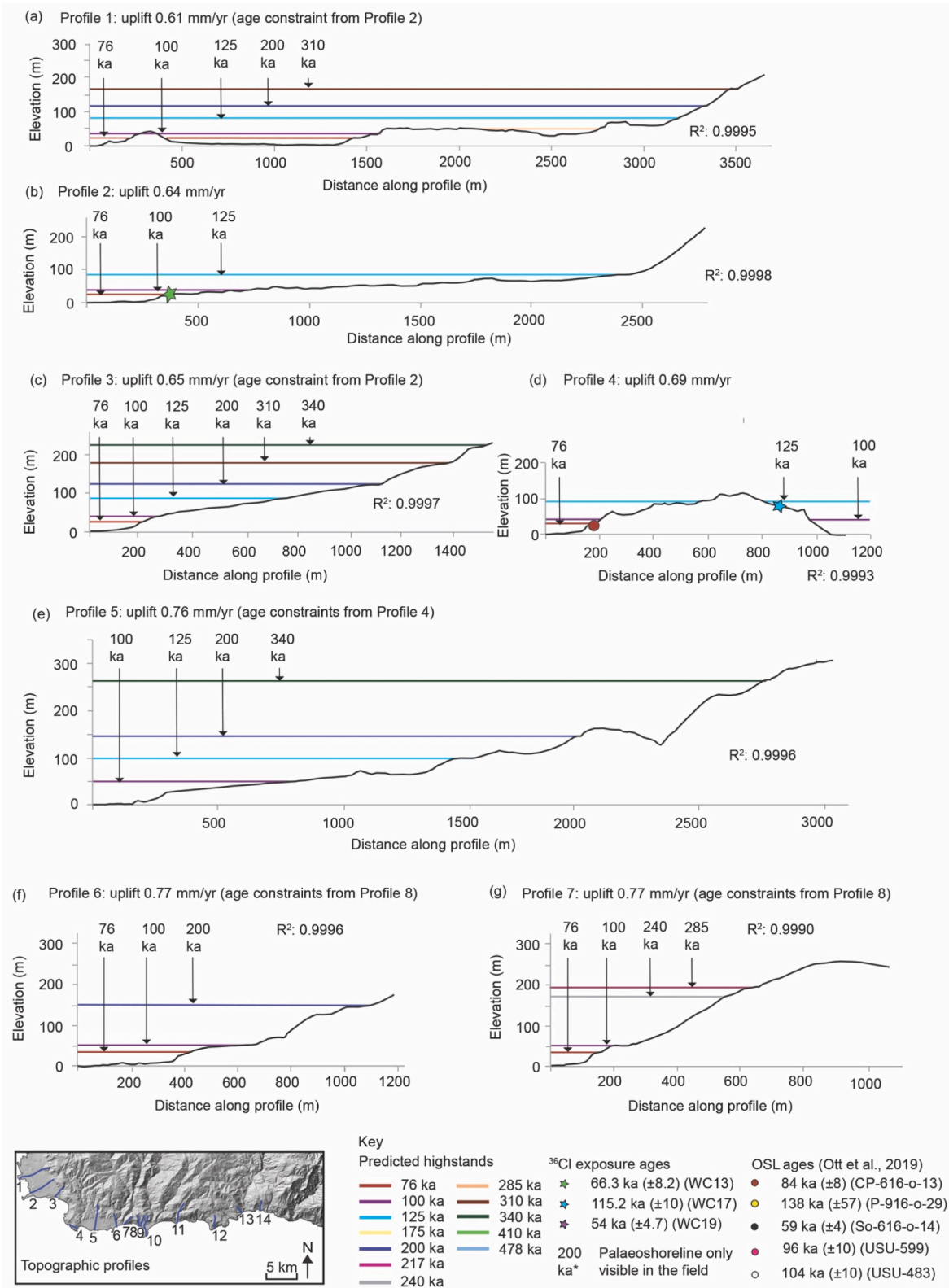
Fig. 7. (a–m) Topographic profiles for Profiles 1–14. Measured palaeoshorelines are matched to highstand elevations predicted by the Terrace Calculator given an iterated uplift rate and ^{36}Cl exposure ages alongside OSL ages from Ott et al. (2019). Two uplift rate scenarios for P14 (n, m) are presented, see text for details. (o) R^2 for measured to predicted palaeoshoreline elevations of 0.9991 for P1-13. (p) Continuity of palaeoshorelines visible on the DEM between P6–P10.

(h) Profile 8: uplift 0.75 mm/yr

(i) Profile 9: uplift 0.75 mm/yr (age constraints from Profile 10)

(j) Profile 10: uplift rate 0.76 mm/yr

(k) Profile 11: uplift rate 0.83 mm/yr (age constraints from Profile 10)

Key

Predicted highstands

76 ka	240 ka
100 ka	285 ka
125 ka	310 ka
175 ka	340 ka
200 ka	410 ka
217 ka	478 ka

Topographic profiles   5 km

^{36}Cl exposure ages

66.3 ka (±8.2) (WC13)
115.2 ka (±10) (WC17)
54 ka (±4.7) (WC19)

200 ka*   Palaeoshoreline only visible in the field

OSL ages (Ott et al., 2019)

84 ka (±8) (CP-616-o-13)
138 ka (±57) (P-916-o-29)
59 ka (±4) (So-616-o-14)
96 ka (±10) (USU-599)
104 ka (±10) (USU-483)

Fig. 7. (*continued*).

P10, Ott et al. (2019) obtain three OSL age controls that they use to correlate the 56–58 m palaeoshoreline with the 100 ka highstand of MIS 5c (138 (±57) ka Sample P-916-o-29, 96 (±10) ka Sample USU-599 and 104 (±10) ka Sample USU-483) (Figs. 2, 7 h-j). Uplift rates of 0.75, 0.75 and 0.76 mm/yr on P8, P9 and P10, respectively, are required for this correlation. On P10 we obtain a ^{36}Cl exposure age of 54 (±4.7) ka for

sample WC19 removed from the 22 m wave cut platform (Figs. 2, 4 and 5, 7j), note that because the topography north and landward of P10 decreases to 5–10 m it is not possible to determine the palaeoshoreline elevation associated with the 22 m platform. Therefore, we model the uplift rate associated with WC19 using the sample elevation. Sample WC19 associates the 22 m wave-cut platform with a highstand within

Fig. 7. (*continued*).

MIS 3c and is explained by an uplift rate of 1.4 mm/yr. Unfortunately, it is clear that the palaeoshoreline to highstand correlations inferred from the OSL and ^{36}Cl age controls from P8–P10 cannot all be explained using the same rate of uplift. To determine the uplift rates on P8–P10 we use the terrace calculator to first interrogate whether the age contr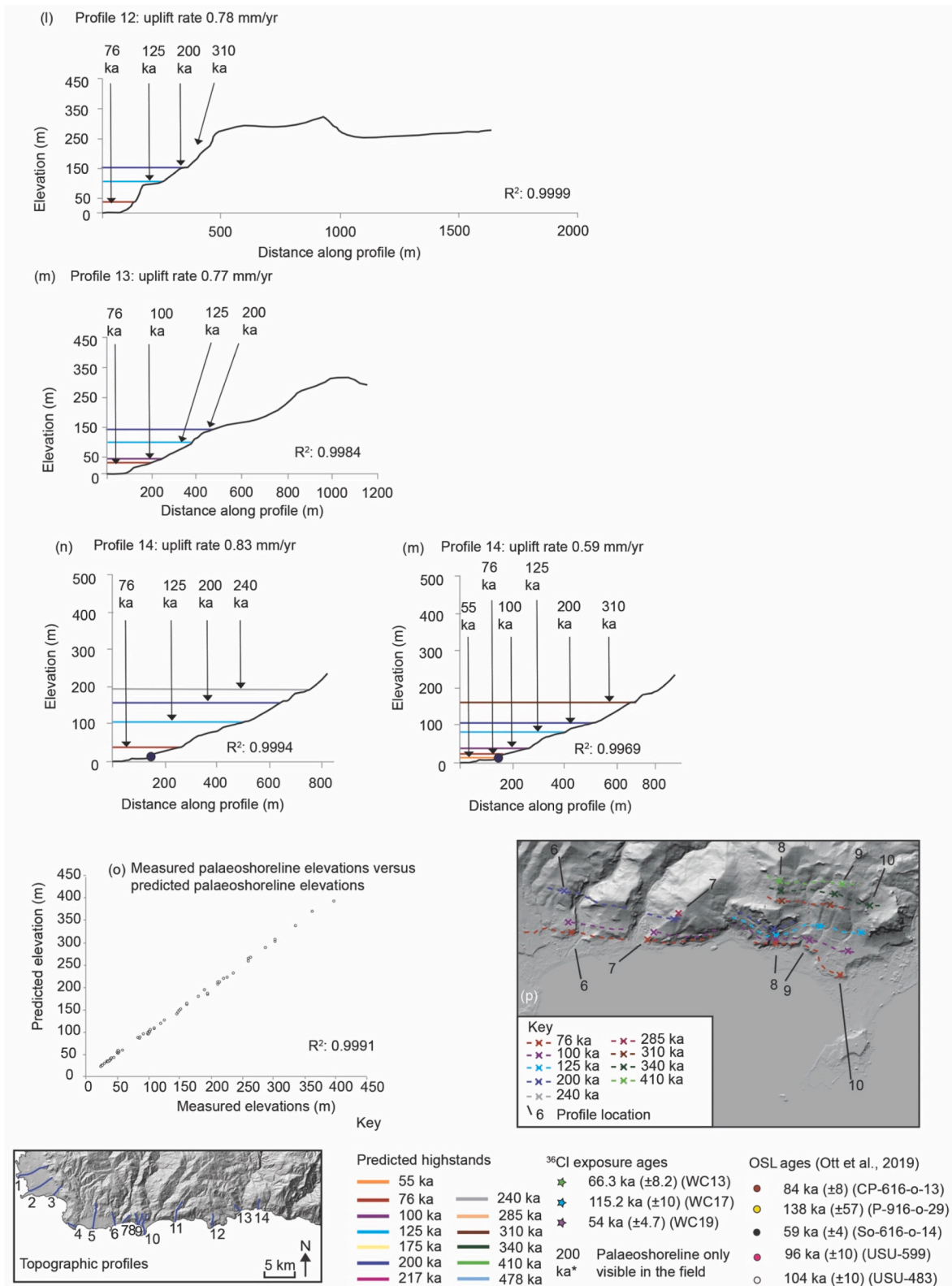ols can be explained using an uplift rate that changes through time. If a changing uplift rate is not a viable solution, we use the terrace calculator to identify which of the uplift rates from the age controls results in the best fit of measured to predicted palaeoshoreline elevations. This approach uses the terrace calculator to identify the number of matches made between measured and predicted palaeoshoreline elevations obtained from using the uplift rates (0.5, 0.76, 1.4 mm/yr) determined by the age controls. For each uplift rate attempt, the number of matches between measured and predicted palaeoshorelines can be used to infer the best fit uplift rate (see Section 3.4). We find that a change in uplift rate cannot explain the age controls associated with the 14 m and 56–58 m palaeoshorelines and the 22 m wave-cut platform on P8–P10. Analyses using the terrace calculator to investigate the uplift rates obtained using each of the age controls on P8–P10 (Supplementary data Table 2) reveal that the 56–58 m palaeoshoreline allocated to the 100 ka highstand yields the greatest number of matches (seven) between measured and predicted palaeoshorelines compared to four and two matches obtained using the 76 ka palaeoshoreline at 14 m and 55 ka wave-cut platform at 22 m, respectively. Thus, we use the correlation of the 100 ka palaeoshoreline at 56–58 m along P8-10 within our uplift modelling (Fig. 7h–j, p). We briefly consider the 54 (±4.7) ka ^{36}Cl exposure age of WC19 that we associate with the MIS 3c**.** We do not think that the 54 (±4.7) ka ^{36}Cl age control on the 22 m platform is erroneously young due to erosion because the sampling location of WC19 displayed low erosion indicators of up to 1.5 cm deep vertical lithophagid borings and millholes (Fig. 4o). When we modelled WC19 for uplift associated with the 55 m highstand (MIS 3c) we used a sea-level elevation of −55 m relative to today (Siddall et al., 2003). However, significant variability (~44 m) exists in the postulated MIS 3c sea-level elevations (e.g., elevations from −18 to −62 m relative to today using Lambeck and Chappell, 2001; Waelbroeck et al., 2002; Siddall et al., 2003; Bates et al., 2014; Rohling et al., 2014; Shakun et al., 2015; Spratt and Lisiecki, 2016; Antonioli et al., 2021; Gowan et al., 2021). It is pertinent that two recent studies (Antonioli et al., 2021; Gowan et al., 2021) suggest that the elevation of MIS 3c may be higher than indicated (−18 m to −30 m) from previous studies. We note that if the sea-level elevation during MIS 3c was toward the higher value of this published range, the uplift rate required to elevate the 22 m wave-cut platform hosting WC19 would be lower. Specifically, modelling the 55 m highstand with a sea-level elevation of −18 m necessitates an uplift rate of 0.73 mm/yr. This value is notably close (0.03 mm/yr lower) to the uplift rate obtained from the 100 ka age controls (0.76 mm/yr) used for correlating palaeoshorelines to highstands from P8–P10.

In the eastern extent of our study area, from P11 to P14, one age constraint exists. The OSL age of 59 (±4) ka (Sample So-616-o-14) from Ott et al. (2019) was removed from the 14 m palaeoshoreline 1.5 km east of P13 and 1 km west of P14 (Fig. 2). Ott et al. (2019) associate the 14 m palaeoshoreline in this area with MIS 4 (~60 ka), but it may also be associated with MIS 3c (55 ka highstand) within error. Correlating the 14 m palaeoshoreline dated by Ott et al. (2019) with MIS 3c using the sea level elevation from Siddall et al. (2003) can be explained using an uplift rate of 1.22 mm/yr and results in two matches between measured and predicted palaeoshoreline elevations (Supplementary data Table 3). We also modelled an uplift rate for P14 of 0.59 mm/yr using the age control from Ott et al. (2019) and the sea-level elevation for MIS 3c from Antonioli et al. (2021). Given the uncertainty regarding the sea level elevation during MIS 3c, we were interested to see if a greater number of

matches between measured and predicted palaeoshorelines could be obtained if uplift modelling did not use the 59 (±4) ka age constraint from Ott et al. (2019) on P14. This modelling allocates, in turn, the lowest measured palaeoshoreline to each highstand on the calculator, applying the resultant uplift rate to the topographic profile and matching the measured palaeoshorelines to the predicted palaeoshorelines. For each attempt, the number of matches between measured and predicted palaeoshorelines, the R^2 and the RMSE were used to identify the best fit uplift rate. This model scenario yielded an uplift rate of 0.83 mm/yr. The palaeoshoreline to highstand correlations for the three uplift scenarios are shown in Supplementary Table 3. The outcome of the uplift modelling on P14 shows that four and five highstand to palaeoshoreline correlations can be made for scenarios using the uplift rates of 0.83 mm/yr and 0.59 mm/yr, respectively. We opt present both scenario models for P14 (Fig. 7n, m, 8, 9) to illustrate the uplift rate uncertainty in the east of the study area.

We observe that the elevations of the palaeoshorelines measured in the field and on the DEM achieve a good fit to palaeoshoreline elevations predicted in the terrace calculator given uplift rates obtained using the ^{36}Cl exposure and OSL dated palaeoshorelines discussed above (Fig. 7a-m, summarised in 7o, Table 3). Specifically, R^2 goodness of fit values obtained from plotting the measured versus predicted elevations of palaeoshorelines achieve values above 0.9975 for each topographic profile (Fig. 7a-m, Table 3). The correlations indicate that the uplift rates appear to have been constant throughout the Late Quaternary and that we have successfully assigned undated palaeoshorelines to sea-level highstands observing that some of the most prominent highstands on the sea-level curve (125 ka, 200 ka, 310 ka and 340 ka) are correlated with palaeoshorelines visible on the topographic profiles. Specifically, between P1 and P13 (we exclude P14 in this analysis because we present two uplift scenarios) palaeoshorelines associated with MIS 5a (76 ka) and MIS 5e (125 ka) are identified throughout 11 of the topographic profiles, MIS 5c (100 ka) palaeoshorelines are identified throughout 12 of the profiles, MIS 7a (200 ka) palaeoshorelines have been interpreted on 9 profiles, and correlation is also made between higher and older palaeoshorelines up to 478 ka (Figs. 7 and 8b, Table 3). Continuity of the palaeoshorelines is particularly visible on the DEM between P6–P10 (Paleochora area) when we plot the inferred along-strike palaeoshoreline elevations (Fig. 7p).

Our age controls and correlation modelling also allow us to comment on low elevation (<18 m) palaeoshorelines that occur below palaeoshorelines allocated to the 76 ka (MIS 5a) highstand (Table 3). Specifically, we note that when we model the uplift rates on P4, 8, 10 and 14 using palaeoshoreline elevations and the age controls (obtained herein and those from Ott et al. (2019)), we observe that there are palaeoshorelines between 12 and 18 m located below the 76 ka palaeoshoreline and above the 365 CE notch. This observation raises questions regarding the ages of the 12–18 m palaeoshorelines. On P10 we observed that the dated 22 m wave cut platform can be modelled with a sea level elevation of −18 m for MIS 3c from Antonioli et al. (2021) using an uplift rate almost identical to that used to model the dated 100 ka palaeoshoreline on the same profile. This inspired us investigate the predicted palaeoshoreline elevations of the 55 ka (MIS 3c) highstand across the study area using a −18 m sea-level elevation. Our findings are documented in Table 3 and show that 12-18 m palaeoshorelines may be associated with the sea-level highstand of MIS 3c and/or expected to be Holocene in age using sea-level curve data from Antonioli et al. (2021). In detail we find that the 17 m and 18 m palaeoshorelines on P4 and P8, respectively could belong to MIS 3c along with the 22 m platform on P10. We speculate that the 12 m palaeoshorelines on P4 and P8 and the 16 m palaeoshoreline on P10 may therefore be Holocene in age (Table 3). Note that because of the
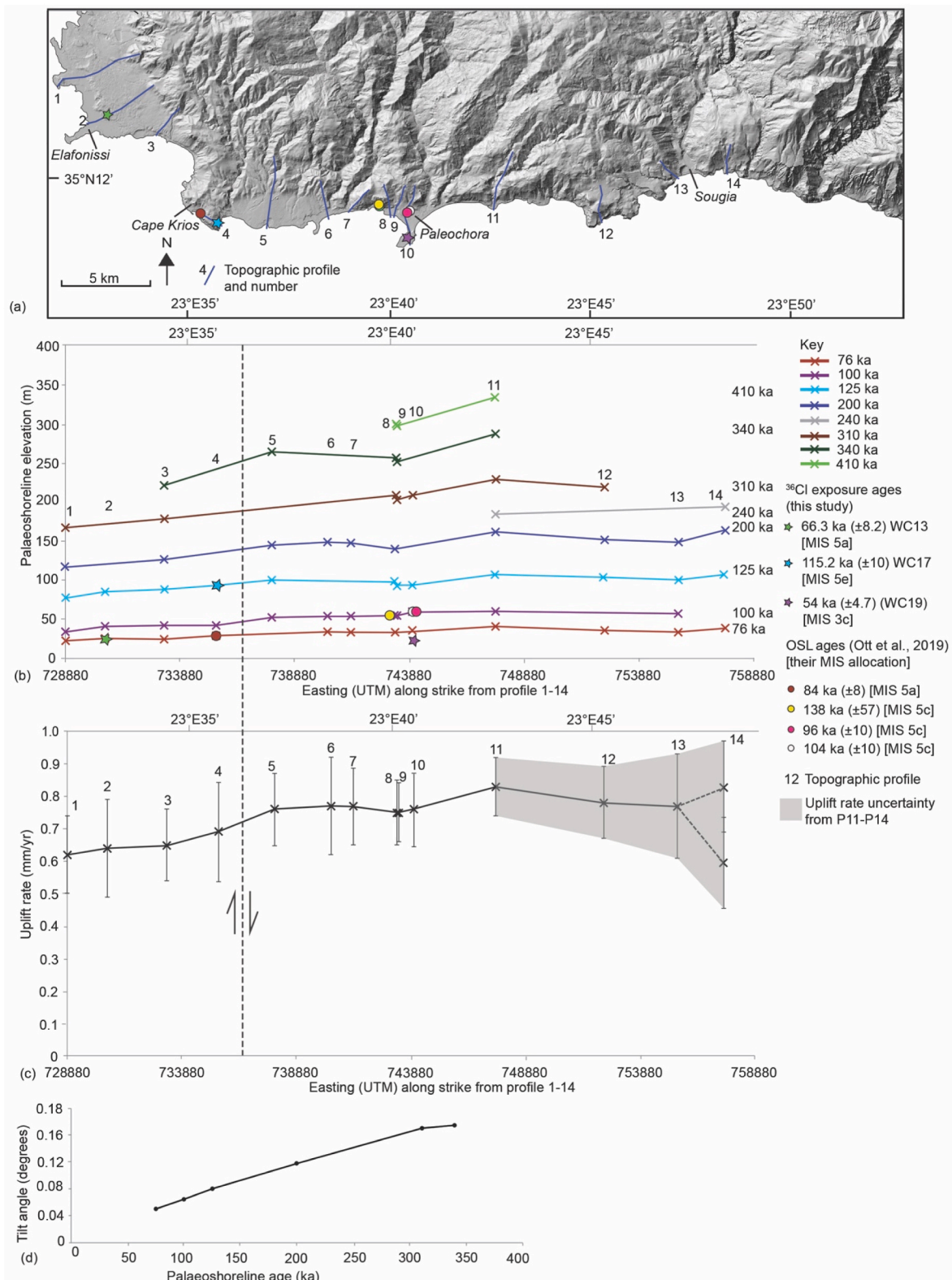
Fig. 8. (a) DEM showing the locations of profiles, ^{36}Cl exposure ages and OSL ages (Ott et al., 2019). (b) Along strike palaeoshoreline elevations for sea-level highstands from 76 ka to 410 ka showing an elevation increasing from P1 in the west to P11 in the east. (c) Uplift rates obtained from analyses of the topographic profiles in Fig. 7. Note that for P14, two uplift rate scenarios are illustrated (see Table 3). Uplift rate uncertainty is illustrated from P11–P14 because of a lack of age controls and the two possible uplift rate scenarios at P14. Dashed line is the location of a localised fault (Ott et al., 2019) suggested to exist between P4 and P5, see text for discussion (d) Tilt angles for each palaeoshoreline show that older palaeoshorelines are more tilted than younger palaeoshorelines. The tilt angles are calculated using the length of each palaeoshoreline from the lowest uplift location profile (P1) to the highest uplift location profile (P11) and the change in elevation from P1–P11. Note that tilt angles for the 240 ka and 410 ka palaeoshorelines cannot be calculated owing to a lack of along strike measurements.

uncertainty associated with MIS 3c sea level elevations these highstand to palaeoshoreline correlations are not included in the R² or RMSE calculations in Fig. 7 and Table 3.

4.4. Spatial uplift rate variation

Palaeoshoreline to sea-level highstand correlations along P1-14 can provide insight into the along-strike deformation, and consequently into the possible causal faulting mechanisms associated with the deformation. Specifically, we interrogate how the palaeoshoreline elevations change along strike, the spatial pattern of Late Quaternary uplift rate change and, the along strike tilt angles of each palaeoshoreline. Spatially from P1 in the west to P11 in the east there is an increase in the elevations of all identified palaeoshorelines (Fig. 8). For example, the 125 ka palaeoshoreline is at 78 m in the west (P1) compared to 108 m in the east (P11). An eastward decrease in palaeoshoreline elevations is evident from P11 to P13, while at P14, depending on whether the age control from Ott et al. (2019) is used the palaeoshorelines may either increase or continue to decrease. The spatial variation in palaeoshoreline elevations suggests uplift rates that increase from 0.61 (±0.12) mm/yr at P1 to 0.83 (±0.14) at P11 (Fig. 8c) then decrease slightly to 0.77 mm/yr at P13. At P14 uplift rates may either be 0.83 mm/yr or 0.59 mm/yr.

The impact of any minor onshore faults in the study area needs to be considered. We suggest that a minor ~ N–S trending, east dipping fault observed by Ott et al. (2019) (Figs. 2c and 8b) between P4 – P5 may only slightly perturb the uplift rates local to the fault, possibly contributing to the uplift on P4 and counteracting the uplift on P5. Specifically, we observe that Fig. 8 shows that from P4 – P5 the 76 ka and older palaeoshorelines demonstrate increasing elevations which may imply that the hangingwall palaeoshorelines have not accommodated significant fault-related subsidence. Ott et al. (2019) also suggest the presence of a ~N–S trending, west dipping normal fault in the vicinity of our P13 and P14, though we do not know exactly where the fault is because it is not on our geological map and was not observed in the field. Accepting the presence of the fault, it may contribute to the uplift observed on P14 and counteract the uplift at P13 but we cannot quantify the impact of the fault. We do not think either of the faults significantly impact the spatial pattern of uplift that we observe throughout the study area.

The change in uplift rates over a length scale of ~30 km is comparable to that seen elsewhere on palaeoshorelines throughout the World that have been deformed due to faulting (e.g., Armijo et al., 1996; Roberts et al., 2009; Saillard et al., 2011; Roberts et al., 2013; Matsu'ura et al., 2014, 2015; Binnie et al., 2016; Jara-Muñoz et al., 2017; Meschis et al., 2018; Robertson et al., 2019; Litchfield et al., 2020). Along-strike tilt angles on deformed palaeoshorelines can be used to investigate whether spatial uplift rate variation can be attributed to faulting (Armijo et al., 1996; Ortlieb et al., 1996; Roberts et al., 2009; Meschis et al., 2018; Normand et al., 2019; Robertson et al., 2019). The tilt angles for each palaeoshoreline are calculated using trigonometry and measurements of the distance where the lowest uplift rate occurs (P1) to where the highest uplift rate occurs (P11), and the elevation difference between the lowest and highest uplift rates (or close to the assumed fault tip and centre). Analysis of the tilt angles of the palaeoshorelines in the study area shows increasing tilt angles with increasing palaeoshoreline age (Fig. 8d). We suggest that the variation in tilt angles occurs because palaeoshorelines deformed by faulting record the cumulative effect of earthquake displacement gradients that are higher in the centre of a fault and decrease toward the tips. As such, older palaeoshorelines display higher tilt angle gradients because they have experienced a longer uplift history compared to younger palaeoshorelines. Although we appreciate this is a rather simplistic view where multiple possible causal faults occur, we suggest that our observations on the length scale of the spatial increase in elevation and uplift rates from west to east over ~20 km combined with increasing tilt angles support the assertion that faulting may be responsible for the observed deformation. Furthermore,

we can conclude that whatever the exact location and kinematics of the dominant fault(s), they have been active after MIS 5a (76 ka highstand) because this palaeoshoreline has been deformed since its formation (Fig. 8b).

4.5. Coseismic vertical deformation patterns

In this section, we establish the patterns of vertical coseismic uplift that may be caused by slip on the subduction interface and faults suggested to be present in southwestern Crete. We adopt this approach because coseismic vertical deformation modelling can be used as a proxy for the expected pattern of long-term vertical deformation (e.g., Robertson et al., 2019). Published models of vertical coseismic deformation from slip on a crustal reverse fault from Shaw et al. (2008) and on the subduction interface from Ganas and Parsons (2009) are displayed in Fig. 9b. To obtain models of coseismic vertical deformation associated with extensional faulting we undertake elastic-half space dislocation modelling using the Matlab code of Mildon et al. (2016) and Coulomb 3.4 software (Toda et al., 2011) (Section 3.5) using fault traces from Mascle et al. (1982); Kreemer and Chamot-Rooke (2004), Alves et al. (2007); Kokinou et al. (2012), and Sakellariou and Tsampouraki-Kraounaki (2019)). These studies suggest south-dipping extensional faults located within ~5 km of the shoreline of Paleochora (Fig. 2) that coincide with a bathymetric trough. However, the extent and number of extensional faults do not agree between studies. For example, the length of the fault traces from Kreemer and Chamot-Rooke (2004), Kokinou et al. (2012) and, Sakellariou and Tsampouraki-Kraounaki (2019) are 70 km, 29 km and 52 km, respectively. In comparison, Alves et al. (2007, 2014) and Mascle et al. (1982) identify multiple, relatively shorter offshore faults along strike from one another. We also note that Sakellariou and Tsampouraki-Kraounaki (2019) argue that the fault zone south of southwestern Crete may host dextral sense of motion and we model their fault trace with normal and transtensional dextral strike slip motions. We model each of the single fault traces (Kreemer and Chamot-Rooke, 2004; Kokinou et al., 2012; Sakellariou and Tsampouraki-Kraounaki, 2019) as they are presented in the original studies (green lines, Fig. 9i-l). For the studies that identify multiple but relatively shorter fault traces (Mascle et al., 1982; Alves et al., 2007, 2014) we model several fault rupture scenarios (Fig. 9c–h; Table 4) because the distance between the tips of their along strike faults are relatively short (~3–6 km) and knowledge of fault behaviour (e.g., Fossen and Rotevatn, 2016) tells us that closely spaced along strike faults may be segmented at the surface but linked at depth. We do not model the exact normal east-west fault trace used by Ott et al. (2021) because we opt to use fault traces presented in the original studies. However, we note that the ~100 km long east-west fault from Ott et al. (2021) is similar in location and length to the modelled fault trace 'Mascle 2' (Fig. 9h).

The coseismic vertical deformation for the reverse crustal splay fault (Shaw et al., 2008), slip on the subduction interface (Ganas and Parsons, 2009) (Fig. 9b) and those obtained from modelling the extensional faults (Fig. 9c-m) can be examined along strike. The plots of coseismic uplift (Fig. 9b, m) reveal two key observations. Firstly, we observe that maximum coseismic uplift of the coastline for the reverse faulting earthquakes in the studies of Shaw et al. (2008) and Ganas and Parsons (2009) is significantly higher (2.25–8.5 m) than the maximum coseismic uplift values from the extensional faults (0.03–0.5 m) (Fig. 9c-m). This observation is expected given that modelled ruptures on the reverse faults were intended to produce earthquakes Mw > 8, whereas the earthquake magnitudes (Mw < 7.2; Table 4) on the extensional faults were dictated by the scaling relationships using the length of the fault traces. Secondly, there is variation in the spatial pattern of coseismic uplift between the reverse and extensional faults. In more detail, the coseismic uplift modelled by Shaw et al. (2008) and Ganas and Parsons (2009) for a 365 CE earthquake on a reverse upper-plate splay fault and slip on the subduction interface, respectively, reveals spatial uplift
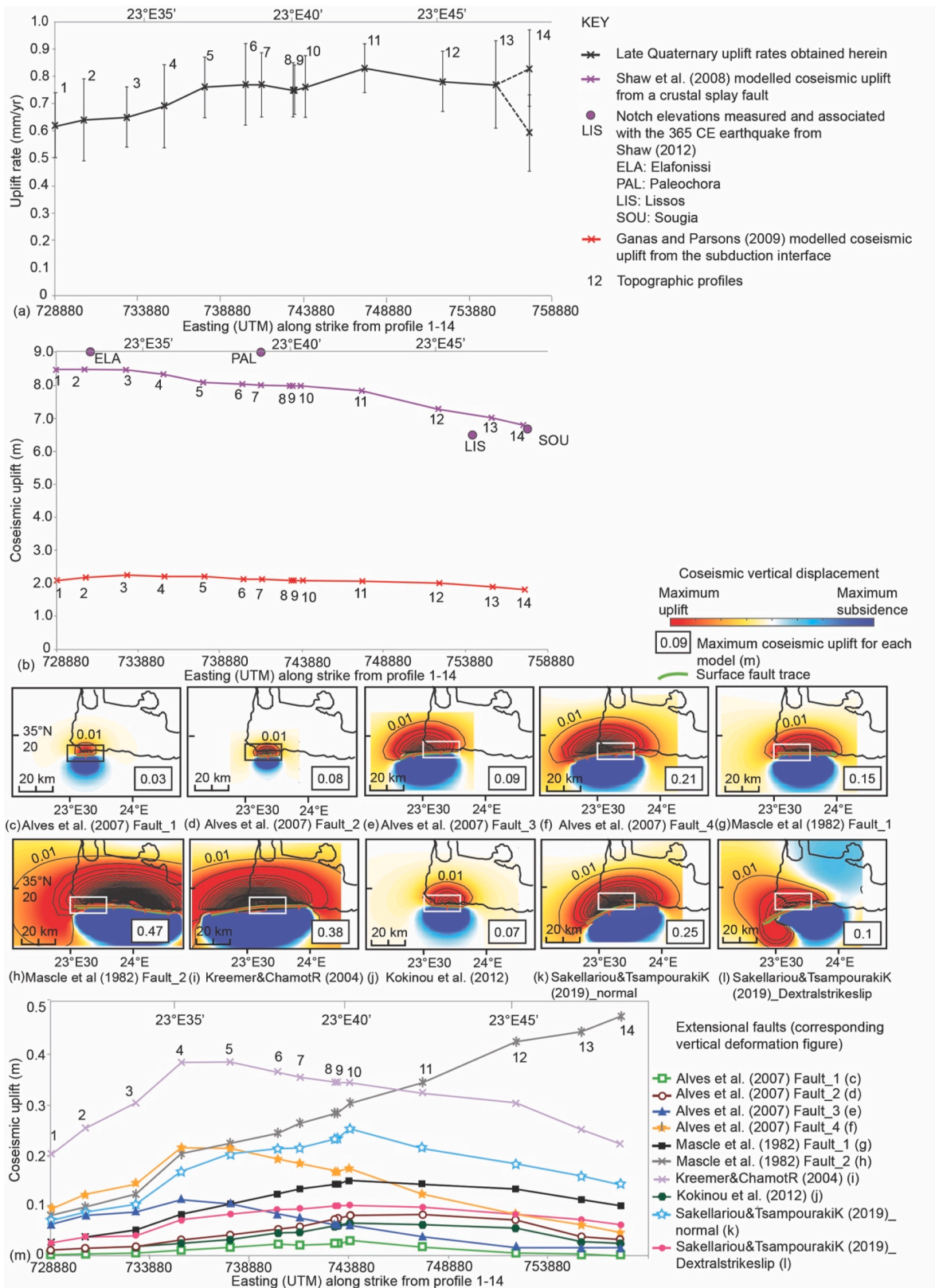
Fig. 9. (a) Late Quaternary uplift rates for P1–P14. (b) Modelled coseismic uplift from Shaw et al. (2008) and from Ganas and Parsons (2009) for earthquakes on a crustal reverse fault and the subduction interface, respectively (see Fig. 1c). (c–l) Coseismic vertical displacement modelled using Coulomb according to extensional fault traces from the studies of Alves et al. (2007), Mascle et al. (1982), Kreemer and Chamot-Rooke (2004), Kokinou et al. (2012) and Sakellariou and Tsampouraki-Kraounaki (2019) (see Table 4 for modelling values). The green line on each displacement model is the surface trace of the ruptured fault. Each contour represents 0.01 m of coseismic uplift, the maximum coseismic uplift for each model is displayed. (m) Along strike modelled coseismic vertical uplift obtained from (c–l) for fault traces.

Table 1

DEM and field measurements of palaeoshorelines from this study and from 2023).(Ott et al., 2019,

Profile reference	DEM palaeoshoreline elevations (this study) (m)	Barometric altimeter palaeoshoreline elevations (this study) (m)	Palaeoshoreline elevations (Ott et al., 2019, 2023) (m)
1	22		
	35		*30–40*
	78		
	118		
	167		
2	25	24	
	40		*30–40*
	85		
3	25		
	41		
	88		
	126		
	179		
	222		
4		12	
		17	16
	29		27
	42	44	40
	91	91	83
5	52		
	100		
	144		
	266		
6			16
	33		
	53		56
			107
	148		
7			11
	33		39.5
			43
	54		55
			61
			76
	177		
	194		
8		12	14
		18	19
	33		34
	54	56	56
			75
	98	95	
	140	140	
	211	206	
	258		
	306		
9	53		
	95		
	206		
	264		
	302		
10		16	
		22	
	34		
	58		
	95		
	211		
11			13
			21.5
	40		40
	59		
	108		
	162		
	185		
	231		
	288		
	337		
	392		
12	35		
	104		
	151		
	219		

Table 1 (*continued*)

Profile reference	DEM palaeoshoreline elevations (this study) (m)	Barometric altimeter palaeoshoreline elevations (this study) (m)	Palaeoshoreline elevations (Ott et al., 2019, *2023*) (m)
13	33		
	56		
	100		
	148		
14		12	12
			20
	38		
	108		
	164		
	192		

patterns that decrease from west to east within the research area (Fig. 9b). The coseismic uplift model of Shaw et al. (2008) suggests highest uplift (~8.5 m) occurred at P1, decreasing eastward toward P14. Lower coseismic uplift values are observed from the model of Ganas and Parsons (2009) with maximum uplift (2.25 m) at P4 decreasing to the east. Comparing the coseismic uplift modelled using extensional fault traces from Mascle et al. (1982); Kreemer and Chamot-Rooke (2004), Kokinou et al. (2012), Alves et al. (2007) and Sakellariou and Tsampouraki-Kraounaki (2019) reveals a variety of spatially variable uplift patterns (Fig. 9m). Specifically, the coseismic uplift patterns generated by earthquakes using the fault traces of Kreemer and Chamot-Rooke (2004) (Fig. 9i) and faults 3 and 4 from Alves et al. (2007) (Fig. 9e and f) reveal coseismic uplift that increases from P1 to a maximum value at P4 and then decreases from P4 to P14 (Fig. 9m). We observe that the combination of five faults from Mascle et al. (1982) (labelled Fault_2, Fig. 9h) results in coseismic uplift that steadily increases from P1 to P14 (Fig. 9m). The coseismic uplift patterns produced by rupturing faults from Sakellariou and Tsampouraki-Kraounaki (2019) (Fig. 9k for a normal fault and 9l for a dextral transtensional fault), Kokinou et al. (2012) (Fig. 9j), fault 1 from Mascle et al. (1982) (Fig. 9g) and faults 1 and 2 from Alves et al. (2007) (Fig. 9c and d) reveal similar spatial uplift patterns where uplift increases from P1 in the west towards P10/11, after which it slightly decreases toward P14. We consider the patterns of coseismic uplift from the reverse and extensional fault traces in context with the Late Quaternary spatial uplift rate pattern in the discussion.

To summarise the results presented herein, we find that ^{36}Cl exposure ages and existing OSL ages can be used to infer that southwestern Crete has been uplifting at a temporally constant rate throughout the Late Quaternary since ~400 ka. The palaeoshoreline elevations and Late Quaternary uplift rates increase from the western corner of Crete (0.61 ± 0.12 mm/yr) to a maximum at P11 (0.83 ± 0.14 mm/yr) then decrease to 0.77 mm/yr at P13. Depending on the scenario accepted at P14, the uplift rates may continue to decrease to 0.59 mm/yr or increase to 0.83 mm/yr. Moreover, along-strike tilting during uplift over a length-scale of 20 km indicates that the dominant mechanism of uplift is likely to be related to the displacement gradient of an active fault(s). Our coseismic vertical deformation modelling of extensional fault traces obtained from the literature reveal a variety of spatial vertical uplift patterns. When the extensional coseismic uplift patterns are compared to coseismic uplift patterns from ruptures on the postulated crustal splay fault from Shaw et al. (2008) and slip on the subduction interface from Ganas and Parsons (2009) there are variations in the magnitude of vertical deformation and in the spatial patterns of the deformation.

5. Discussion

Although southwestern Crete has been the focus of numerous fault-related uplift studies (e.g., Shaw et al., 2008; Ganas and Parsons,

2009; Tiberti et al., 2014; Mouslopoulou et al., 2015b; Ott et al., 2019, 2021) there continues to be debate regarding the dominant long term faulting mechanism which confounds attempts to adequately define the potential seismic hazard. In this section we attempt to infer which fault (s) may contribute to Late Quaternary uplift of the southwestern coastline of Crete. We do this by comparing the Late Quaternary uplift pattern obtained herein with patterns of coseismic uplift from slip on the subduction interface, the postulated crustal reverse fault and slip on the extensional faults. A clear contrast is visible when we compare the patterns of Late Quaternary uplift rates determined herein using palaeoshorelines (Fig. 9a) with the coseismic vertical uplift patterns modelled from slip on the subduction interface (Ganas and Parsons, 2009) and a crustal reverse fault constrained using Holocene notch data (Shaw et al., 2008) (Fig. 9b). Specifically, the uplift rates on Late Quaternary palaeoshorelines increase from west to east until P11 and appear to then decrease from P11 to P13, this is compared to the coseismic uplift from slip on the reverse/subduction faults that decrease from west to east. If the 365 CE earthquake is associated with slip on either the subduction interface or an upper plate reverse fault, and activity on this fault dominates the deformation in southwestern Crete, we expect that multiple 365 CE-type events with similar slip distributions through time would produce higher uplift in the west decreasing to lower uplift in the east, this pattern is not reflected in the Quaternary uplift rate pattern. Thus, accepting the spatial pattern of Late Quaternary uplift presented herein using cosmogenic and OSL age constraints, we suggest that sustained slip on the subduction interface and/or a reverse crustal splay fault as modelled by Shaw et al. (2008) and Ganas and Parsons (2009) are unlikely to be the sole cause of long-term uplift pattern observed herein.

Extensional tectonics are reported to dominate the shallow deformation onshore and offshore Crete where sustained footwall uplift from extensional faults has been purported to be responsible for the observed Late Quaternary deformation of sequences of palaeoshorelines throughout the eastern, southern and western coastlines (Gaki-Papanastassiou et al., 2009; Caputo et al., 2010; Robertson et al., 2019; Ott et al., 2019; 2021). Thus, it is a plausible explanation that the extensional fault(s) that bounds the southwestern coastline of Crete may also contribute to uplift observed along the coastline. The relative spatial change in modelled coseismic footwall uplift from each of the extensional fault scenarios can be compared the Late Quaternary uplift rate pattern obtained herein to gain insight into the possible fault trace(s) that may contribute to palaeoshoreline deformation in southwestern Crete. The spatial patterns of coseismic uplift modelled using the fault traces from Kreemer and Chamot-Rooke (2004) (Fig. 9i, m) and faults 3 and 4 from Alves et al. (2007) (Fig. 9e, f, m) (uplift increasing from P1 to an its maximum at P4 and decreasing from P4 to P14) do not agree with the Late Quaternary uplift rate pattern (Fig. 9a). The uplift pattern modelled from Mascle et al. (1982) fault 2 (Fig. 9h), which increases from P1 to P14 may be similar to the Late Quaternary uplift rate pattern

Table 2

^{36}Cl exposure age results for samples WC13, WC14, WC16, WC17 and WC19.

Sample reference	Profile reference	Latitude (°)	Longitude (°)	Elevation (m)	Palaeoshoreline Elevation (m)	Erosion rate (mm/kyr)	Total erosion (mm)	CaO (wt%)	± CaO (wt%)	Cl in sample (p. p.m)	± Cl in sample (p. p.m)	36Cl (g of rock)	±36Cl (g of rock)	Age (kyr)	Total uncertainty (kyr)
WC13	P2	35.276	23.539	22	25	0.2	13	32.93	1.36	125	1.5	1063966	33573	66.3	8.19
WC14	P2	35.276	23.539	30	40	0.2	7	46.11	2.13	85.5	2.1	630450	18551	33.4	3.4
WC16	P8	35.242	23.672	136	140	0.2	7	58.54	0.75	27.3	0.1	626236	23218	33.1	3.1
WC17	P4	35.234	23.590	75	91	0.2	23	38.64	1.83	57.6	0.5	1652868	44680	115.2	9.99
WC19	P10	35.226	23.679	22	22?	0.2	11	39.98	0.52	25.9	0.1	727215	22415	54.0	4.67

if the higher uplift rate scenario at P14 occurs. However, it is worth noting that the magnitude of modelled coseismic uplift from an earthquake on the trace of Mascle et al. (1982) fault 2 increases nearly five-fold from P1 to P14. The same magnitude of uplift is not apparent in the Late Quaternary uplift rate change from P1 to 14, suggesting that earthquakes on a fault trace this long may be unlikely to be responsible for the observed long-term deformation. The coseismic uplift patterns (Fig. 9m) of the fault traces from Sakellariou and Tsampouraki-Kraounaki (2019) (Fig. 9k, l), Kokinou et al. (2012) (Fig. 9j), fault 1 from Mascle et al. (1982) (Fig. 9g) and faults 1 and 2 from Alves et al. (2007) suggest increasing uplift from P1 to P10/11 followed by a slight decrease in uplift toward P14. We interpret that this pattern is broadly similar to the spatial pattern of Late Quaternary uplift rates if the uplift rate at P14 is the lower value. We recognise that our coseismic models do not consider postseismic deformation. However, it has been proposed that the spatial pattern of coseismic and postseismic deformation are similar and that postseismic deformation increases the magnitude of vertical motions by up to a few tens of percent of the coseismic values (Atzori et al., 2009; D'Agostino et al., 2012; Ganas et al., 2022). The Late Quaternary spatial uplift rate pattern using the lower uplift rate scenario at P14 may be interpreted to approximately match the coseismic uplift pattern from several of the investigated fault traces, specifically Mascle et al. (1982) fault 1; Kokinou et al. (2012); Sakellariou and Tsampouraki-Kraounakil (2019). If the higher uplift rate at P14 is applied, only the coseismic uplift pattern from Mascle et al., (1982), fault 2 produces a spatial uplift pattern that is similar to the Late Quaternary uplift rate pattern but we have reservations about the magnitude of coseismic uplift modelled between P1–P14 and what we observe. Our results suggest that slip on a fault associated with at least one of these fault traces may be, in part, responsible for the Pleistocene palaeoshoreline deformation documented herein.

We acknowledge the presence and briefly discuss the impact of two N–S normal faults located on the west of Crete because their deformation fields overlap with the west of the study area. The offshore and onshore faults Phalasarna (Ph) and Western Crete (WC) (Fig. 1c), respectively, both dip west and would produce coseismic uplift that is higher in the southwestern corner of Crete decreasing eastward along the southwestern coastline (e.g., Ott et al., 2021). The Late Quaternary uplift rate pattern observed herein does not reflect this uplift pattern, implying that slip on the Phalasarna and Western Crete faults do not significantly impact the long-term deformation signal along southwestern Crete.

We recognise that it is both plausible and likely that the overall cause of uplift on southwestern Crete is more complex than slip on an east-west trending extensional fault and may also occur as a result of slip on a crustal reverse fault and/or the subduction interface. This is evidenced by a mixture of extensional and compressional fault plane solutions and instrumental seismicity located in the area of southwestern Crete (e.g., Taymaz et al., 1990; Kiratzi and Louvari, 2003; Yolsal-Cevikbilen and Taymaz, 2012; Ganas et al., 2013, 2018; Sachpazi et al., 2020; Ganas et al., 2022). Our findings suggest that the observed long term deformation pattern presented herein can be explained if sustained extensional faulting is interspersed with larger magnitude (Mw > 8) reverse faulting earthquakes on a crustal reverse fault and/or the subduction interface (see Fig. 10 for a schematic illustration). However, we cannot rule out that non-uniform earthquake ruptures on the subduction interface or postulated crustal reverse fault may also contribute to a long-term spatial uplift pattern that varies from coseismic uplift models based on the Holocene notches. In the scenario where uplift is caused by compressional and extensional earthquakes the magnitude and spatial patterns of uplift through time would vary depending on the rupturing fault and the earthquake recurrence intervals on each fault, but we note that extensional earthquake magnitudes up to Mw 7.0 may occur based on the fault length-scaling relationship from Wells and Coppersmith (1994) (for fault traces from Mascle et al., 1982 (fault 1); Alves et al., 2007 (faults 1 and 2); Kokinou et al., 2012; Sakellariou and Tsampouraki-Kraounakil, 2019) and the fact that the 2020 Mw 7 Samos

Table 3

Uplift rates, DEM and field measurements of palaeoshorelines, predicted palaeoshoreline elevations from the Terrace Calculator and measurements from Ott et al. (2019, 2023) for each topographic profile. We show (i) possible Holocene palaeoshorelines that are inferred from our correlation modelling and, (ii) where correlations may be made between the 55 ka (MIS 3c) highstand and palaeoshoreline elevations using a sea-level elevation of −18 m for MIS 3c, informed by Antonioli et al. (2021). As a result of the uncertainty regarding the sea-level highstand of MIS 3c (55 ka) we have not included these highstand to palaeoshoreline correlations in our R^2 and RMSE calculations. All easting and northing references are for Zone 34 S.

Profile reference	Uplift rate (mm/yr)	R2 and RMSE (m)	UTM of altimeter measurements Easting	Northing	Allocated highstand age (ka) [MIS]	Predicted palaeoshore-line elevations (m)	DEM palaeoshore-line elevations (this study) (m)	Barometric altimeter palaeoshore-line elevations (this study) (m)	Palaeoshore-line elevations Ott et al. (2019, 2023)(m)	Age control (Sample, age) *OSL age from Ott et al. (2019)
1	0.61 ± 0.12	0.9995 3.85			76 [5a]	23	22			
					100 [5c]	36	35		*30–40*	
					125 [5e]	81	78			
					200 [7a]	117	118			
					310 [9c]	167	167			
2	0.64 ± 0.15	0.9998 1.00	730914	3906569	76 [5a]	25	25	24		WC13: 66.3 ± 8.2 ka
					100 [5c]	39	40		*30–40*	
					125 [5e]	85	85			
3	0.65 ± 0.11	0.9997 2.92			76 [5a]	26	25			
					100 [5c]	40	41			
					125 [5e]	86	88			
					200 [7a]	125	126			
					310 [9c]	180	179			
					340 [9e]	226	222			
4	0.69 ± 0.15	0.9993 2.03	735929	3902338	Holocene?			12		
			735929	3902338	Holocene/55 [3c]	20		17	16	
					76 [5a]	29	29		27	*CP-616-o-13: 84 ± 8 ka
			735730	3902072	100 [5c]	44	42	44	40	
			735610	3902145	125 [5e]	91	91	91	83	WC17: 115.2 ± 10 ka
5	0.76 ± 0.11	0.9996 3.42			100 [5c]	51	52			
					125 [5e]	100	100			
					200 [7a]	147	144			
					340 [9e]	263	266			
6	0.77 ± 0.15	0.9996 2.23							16	
					76 [5a]	35	33			
					100 [5c]	52	53		56	
					125 [5e]	101			107	
					200 [7a]	149	148			
7	0.77 ± 0.12	0.9990 4.20							11	
					76 [5a]	35	33		39.5	
					?				43	
					100 [5c]	52	54		55	
					?				61	
					?				76	
					200 [7e]	180	177			
					285 [9a]	189	194			
8	0.75 ± 0.1	0.9993 6.91	742668	3902710	Holocene?			12	14	
			742668	3902710	Holocene/55 [3c]	23		18	19	
					76 [5a]	33	33		34	
			743158	3902821	100 [5c]	50	54	56	56	*P-916-o-29: 138 ± 57 ka
									75	
			742989	3902890	125 [5e]	99	98	95		
			743174	3903099	200 [7a]	145	140	140		
			743065	3903269	310 [9c]	211	211	206		
					340 [9e]	260	258			
					410 [11c]	303	306			
9	0.75 ± 0.09	0.9992 7.70			100 [5c]	50	53			
					125 [5e]	99	95			
					310 [9c]	211	206			
					340 [9e]	260	264			
					410 [11c]	303	302			

Table 3 (*continued*)

Profile reference	Uplift rate (mm/yr)	R2 and RMSE (m)	UTM of altimeter measurements Easting	Northing	Allocated highstand age (ka) [MIS]	Predicted palaeoshore-line elevations (m)	DEM palaeoshore-line elevations (this study) (m)	Barometric altimeter palaeoshore-line elevations (this study) (m)	Palaeoshore-line elevations Ott et al. (2019, 2023)(m)	Age control (Sample, age) *OSL age from Ott et al. (2019)
10	0.76 ± 0.13	0.9975 9.63	743835	3901402	Holocene?			16		
			743835	3901402	55 [3c]	24		22 (platform elevation)		WC19: 54 ± 4.7 ka
					76 [5a]	34	34			
					100 [5c]	51	58			*USU-599: 96 ± 10 ka *USU-483: 104 ± 10 ka
					125 [5e]	100	95			
					310 [9c]	214	211			
11	0.83 ± 0.09	0.9993 10.6			Holocene?				13	
					55 [3c]?	28			21.5	
					76 [5a]	39	40		40	
					100 [5c]	58	59			
					125 [5e]	109	108			
					200 [7a]	161	162			
					240 [7e]	194	185			
					310 [9c]	235	231			
					340 [9e]	287	288			
					410 [11c]	335	337			
					478 [13a]	397	392			
12	0.78 ± 0.11	0.9999 1.71			76 [5a]	36	35			
					125 [5e]	103	104			
					200 [7a]	151	151			
					310 [9c]	220	219			
13	0.77 ± 0.16	0.9984 4.63			76 [5a]	35	33			
					100 [5c]	52	56			
					125 [5e]	101	100			
					200 [7a]	149	148			
14 (option 1)	0.83 ± 0.14	0.9994 3.61	756404	3904187	Holocene?			12	12	
					55 [3c]	28			20	
					76 [5a]	39	38			
					125 [5e]	109	108			
					200 [7a]	161	164			
					240 [7e]	194	192			
14 (option 2)	0.59 ± 0.14	0.9969 7.4	756404	3904187	55 [3c]	14		12	12	*So-616-o-14: 60.9 ± 3.9 ka
					76 [5a]	21			20	
					100 [5c]	34	38			
					200 [7a]	113	108			
					310 [9c]	161	164			

Earthquake ruptured a ~40 km fault (Ganas et al., 2021). Future work is needed to investigate the length of the offshore extensional faults and determine the relative magnitude of uplift caused by different fault mechanisms. As this study investigates uplift rates over ~400 ka along a 30 km coastal transect that may be deformed by multiple faults we do not consider that our observations can provide insight into the uplift contribution from sediment underplating (e.g., Gallen et al., 2014; Ott et al., 2019), which is suggested to be observed over temporal scales of >1 Ma (Menant et al., 2020). We therefore acknowledge that a presently unknown contribution from sediment underplating may be included in all our uplift determinations but we do not think that this is a first order control on the spatial uplift rate changes observed herein.

In summary, we suggest that sustained reverse faulting on either the subduction interface and/or a crustal splay fault is unlikely to be the sole cause of the Late Quaternary uplift in southwestern Crete. The cumulative footwall uplift from slip on an extensional fault(s) may be modified by the uplift caused by cumulative slip on a reverse crustal fault and/or the subduction interface. If this were the case, then a significant number of extensional earthquakes with smaller coseismic uplift values and shorter earthquake recurrence intervals may occur in comparison to less frequent, but larger magnitude thrust earthquakes (Fig. 10). This possible explanation has implications on the seismic hazard assessment of the region. While possible 365 CE-type reverse faulting earthquakes and subduction interface earthquakes (>Mw 8) have the capacity to cause significant destruction, recurrence intervals on these faults are expected to be longer compared to the more frequent recurrence intervals on the extensional faults investigated herein. Similar tectonic complexities to those we propose herein have been observed at other subduction zones throughout the world including Japan (e.g., Imanishi et al., 2012; Toda and Tsutsumi, 2013; Matsu'ura et al., 2014, Matsu'ura, 2015), New Zealand (Litchfield et al., 2020), southern Italy (Roberts et al., 2013; Meschis et al., 2018) and South America (Saillard et al., 2011; Binnie et al., 2016; Jara-Muñoz et al., 2017). In these regions combined upper-plate faulting and subduction related

Table 4

Input data for modelling extensional faults in the Matlab code of Mildon et al. (2016) and Coulomb deformation and stress change software (Toda et al., 2011). Mw is calculated as per the length-scaling relationship from Wells and Coppersmith (1994). In the code of Mildon et al. (2016) slip at the surface is set at 0.1 (10%) of the slip value at depth, which is based upon the relationship between surface slip (EMERGEO Working Group, 2010; Vittori et al., 2011) and maximum slip at depth (Walters et al., 2009; Wilkinson et al., 2015) for the Mw 6.3 2009 L'Aquila earthquake, Italy.

Reference in Figure 9	Study	Description of southwestern Crete fault traces used	Length (km)	Dip (°)	Facing direction (°)	Rake (°)	Mw (max)	Seismo depth (km)	Slip at depth (m)	Motion
Alves et al. (2007) Fault_1	Alves et al. (2007)	Central fault trace	13.7	60	180	−90	6.07	15	0.6	Normal
Alves et al. (2007) Fault_2	Alves et al. (2007)	Combination of central and eastern fault traces from paper	25.8	60	170	−90	6.48	15	1.4	Normal
Alves et al. (2007) Fault_3	Alves et al. (2007)	Combination of central and western fault traces from paper	35.4	60	170	−90	6.69	15	2.1	Normal
Alves et al. (2007) Fault_4	Alves et al. (2007)	Combination of western, central and eastern fault traces from paper	48.2	60	170	−90	6.89	15	3.1	Normal
Kreemer and Chamot-Rooke (2004)	Kreemer and Chamot-Rooke (2004)	Fault trace using only offshore part up to the Sfakia coastline	70.1	60	170	−90	7.13	15	4.9	Normal
Mascle et al. (1982) Fault_1	Mascle et al. (1982)	Combined western three fault traces	38.5	60	180	−90	6.74	15	2	Normal
Mascle et al. (1982) Fault_2	Mascle et al. (1982)	Mascle_fault_1 extended to include two faults to the east	76.1	60	180	−90	7.18	15	7	Normal
Kokinou et al. (2012)	Kokinou et al. (2012)	Western Crete offshore fault location from paper	24.6	60	180	−90	6.45	15	1.2	Normal
Sakellariou and Tsampouraki-Kraounaki (2019)_normal	Sakellariou and Tsampouraki-Kraounaki (2019)	Western Crete offshore fault location from paper	52.2	60	170	−90	6.9	15	3.2	Normal
Sakellariou and Tsampouraki-Kraounaki (2019)_dextralSS	Sakellariou and Tsampouraki-Kraounaki (2019)	Western Crete offshore fault location from paper	52.2	70	170	−160	6.9	15	3.2	Dextral strike slip

deformation have been reported to contribute coastal deformation. Future work is needed to allow greater understanding into the potential seismic hazard associated with upper-plate and subduction related faulting throughout this area.

6. Conclusions

New Pleistocene age controls from ^{36}Cl exposure dating of wave-cut platforms, existing OSL age controls combined with uplift modelling suggest that palaeoshoreline uplift rates in southwestern Crete have been temporally constant since ~400 ka. Spatial analysis of Late Quaternary uplift rates indicates that uplift increases from west (0.61 ± 12 mm/yr) to east (0.83 ± 14 mm/yr) and may then decrease along a ~30 km transect of southwestern Crete, which is not consistent with the deformation implied by Holocene notches and vertical coseismic uplift modelled using slip only on a crustal reverse splay fault or on the subduction interface. Elastic half-space modelling implies that footwall uplift caused by slip on an offshore extensional fault(s) capable of producing earthquakes up to Mw 7 may contribute to the long term palaeoshoreline deformation and seismic hazard of the area. Our finding implies that future studies should be cautious when using uplift patterns obtained from investigating only deformed Holocene coastal indicators to infer the causes of long-term deformation.

Author contributions

All authors approved the final version of the manuscript and have made substantial contributions to the enclosed submission, CRediT roles are as follows: Jenni Robertson: Conceptualization, Methodology, Formal analysis, Investigation, Writing – Original Draft, Visualization, Project administration, Funding acquisition.; Gerald Roberts: Conceptualization, Methodology, Investigation, Writing – Review and Editing, Supervision, Project administration, Funding acquisition.; Athanassios Ganas: Investigation, Writing – Review and Editing.; Marco Meschis: Investigation, Writing – Review and Editing.; Delia Gheorghiu: Investigation.; Richard Shanks: Investigation.

Declaration of competing interest

The authors declare that they have no known competing financial interests or personal relationships that could have appeared to influence the work reported in this paper.

Data availability

All data used in the research is presented in the manuscript. The Terrace Calculator is available in Houghton et al., 2003: https://doi.org/10.1029/2003GL018112
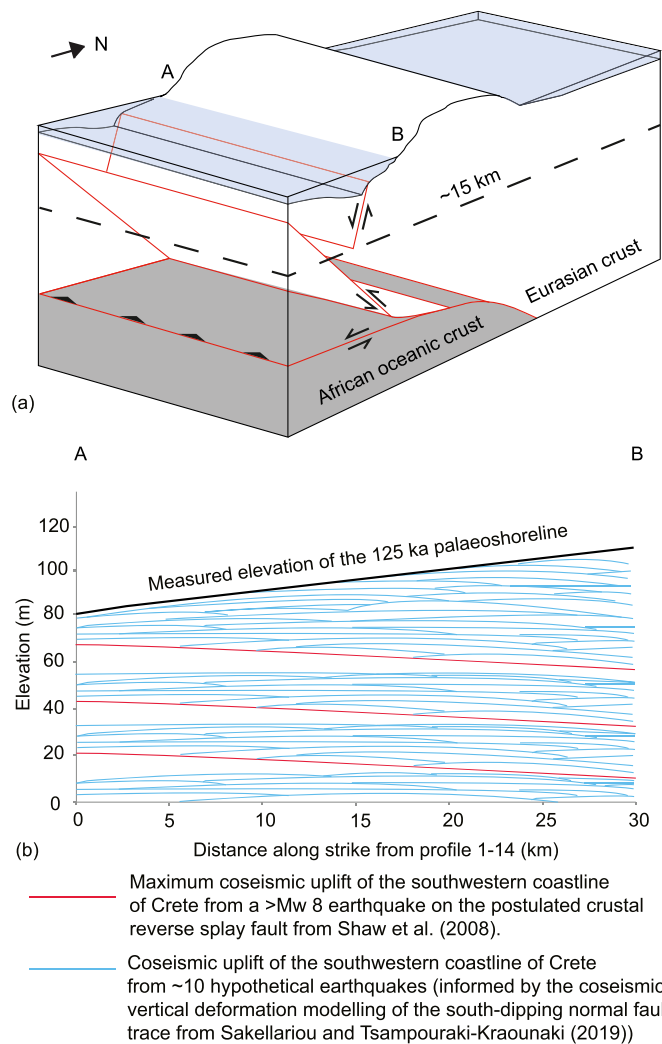
(a)

(b)

— Maximum coseismic uplift of the southwestern coastline of Crete from a >Mw 8 earthquake on the postulated crustal reverse splay fault from Shaw et al. (2008).

— Coseismic uplift of the southwestern coastline of Crete from ~10 hypothetical earthquakes (informed by the coseismic vertical deformation modelling of the south-dipping normal fault trace from Sakellariou and Tsampouraki-Kraounaki (2019))

Fig. 10. (a) 3D cartoon model of the faults that may contribute to palaeoshoreline uplift on the southwestern Crete coastline where A and B represents the locations of P1 and P14, respectively (Fig. 2). Three faults are marked: a low angle subduction interface, an upper plate reverse fault that splays from the subduction interface and an offshore extensional fault that bounds the coastline. (b) Schematic diagram to illustrate that the observed uplift along southwestern Crete over 125 ka may be formed from a combination of many normal faulting earthquakes of varying lengths and magnitudes and very infrequent earthquakes on a reverse fault (we illustrate our point using the coseismic displacement modelled by Shaw et al. (2008) from a rupture on a reverse crustal splay fault). For simplicity, ruptures on the subduction interface are not included in this figure.

Acknowledgements

Appendix A. Supplementary data

Supplementary data to this article can be found online at https://doi.org/10.1016/j.quascirev.2023.108240.

References

Alexander, C.S., 1953. The marine and stream terraces of the Capitola-Watsonville area. University of California Press 10 (No. 1–4).
Alves, T.M., Lykousis, V., Sakellariou, D., Alexandri, S., Nomikou, P., 2007. Constraining the origin and evolution of confined turbidite systems: southern Cretan margin, Eastern Mediterranean Sea (34 30–36 N). Geo Mar. Lett. 27, 41–61.
Alves, T.M., Kokinou, E., Zodiatis, G., 2014. A three-step model to assess shoreline and offshore susceptibility to oil spills: the South Aegean (Crete) as an analogue for confined marine basins. Mar. Pollut. Bull. 86 (1–2), 443–457.
Ambraseys, N., 2009. Earthquakes in the Mediterranean and Middle East: a Multidisciplinary Study of Seismicity up to 1900. Cambridge University Press.
Anderson, R.S., Densmore, A.L., Ellis, M.A., 1999. The generation and degradation of marine terraces. Basin Res. 11 (1), 7–20.
Angelier, J., 1979. Recent Quaternary tectonics in the Hellenic arc: examples of geological observations on land. Tectonophysics 52 (1–4), 267–275.
Antonioli, F., Lo Presti, V.L., Rovere, A., Ferranti, L., Anzidei, M., Furlani, S., et al., 2015. Tidal notches in Mediterranean Sea: a comprehensive analysis. Quat. Sci. Rev. 119, 66–84.
Antonioli, F., Calcagnile, L., Ferranti, L., Mastronuzzi, G., Monaco, C., Orrù, P., et al., 2021. New evidence of MIS 3 relative sea level changes from the Messina Strait, Calabria (Italy). Water 13 (19), 2647.
Armijo, R., Lyon-Caen, H., Papanastassiou, D., 1992. East-west extension and Holocene normal-fault scarps in the Hellenic arc. Geology 20 (6), 491–494.
Armijo, R., Meyer, B.G.C.P., King, G.C.P., Rigo, A., Papanastassiou, D., 1996. Quaternary evolution of the Corinth rift and its implications for the late cenozoic evolution of the aegean. Geophys. J. Int. 126 (1), 11–53.
Atzori, S., Hunstad, I., Chini, M., Salvi, S., Tolomei, C., Bignami, C., et al., 2009. Finite fault inversion of DInSAR coseismic displacement of the 2009 L'Aquila earthquake (central Italy). Geophys. Res. Lett. 36 (15).
Balco, G., Stone, J.O., Lifton, N.A., Dunai, T.J., 2008. A complete and easily accessible means of calculating surface exposure ages or erosion rates from 10Be and 26Al measurements. Quat. Geochronol. 3 (3), 174–195.
Bates, S.L., Siddall, M., Waelbroeck, C., 2014. Hydrographic variations in deep ocean temperature over the mid-Pleistocene transition. Quaternary Sci. Rev. 88, 147–158.
Berryman, K.R., 1993. Distribution, age, and deformation of late Pleistocene marine terraces at Mahia Peninsula, Hikurangi subduction margin, New Zealand. Tectonics 12 (6), 1365–1379.
Binnie, A., Dunai, T.J., Binnie, S.A., Victor, P., González, G., Bolten, A., 2016. Accelerated late quaternary uplift revealed by 10Be exposure dating of marine terraces, Mejillones Peninsula, northern Chile. Quat. Geochronol. 36, 12–27.
Bird, E.C., 2011. Coastal Geomorphology: an Introduction. John Wiley & Sons.
Bradley, W.C., Griggs, G.B., 1976. Form, genesis, and deformation of central California wave-cut platforms. Geol. Soc. Am. Bull. 87 (3), 433–449.
Burbank, D.W., Anderson, R.S., 2013. Tectonic Geomorphology.
Busschers, F.S., Wesselingh, F., Kars, R.H., Versluijs-Helder, M., Wallinga, J., Bosch, J.H.A., et al., 2014. Radiocarbon dating of late Pleistocene marine shells from the southern north sea. Radiocarbon 56 (3), 1151–1166.
Caputo, R., 2007. Sea-level curves: perplexities of an end-user in morphotectonic applications. Global Planet. Change 57 (3–4), 417–423.
Caputo, R., Catalano, S., Monaco, C., Romagnoli, G., Tortorici, G., Tortorici, L., 2010. Active faulting on the island of Crete (Greece). Geophys. J. Int. 183 (1), 111–126.
Choi, K.H., Seong, Y.B., 2021. Constraining the long-term lowering rates of shore platforms on volcanic islands in the East Sea of the Korean Peninsula, using cosmogenic 36 Cl. Geosci. J. 25, 267–281.
D'Agostino, N., Cheloni, D., Fornaro, G., Giuliani, R., Reale, D., 2012. Space-time distribution of afterslip following the 2009 L'Aquila earthquake. J. Geophys. Res. Solid Earth 117 (B2).
De Santis, V., Scardino, G., Meschis, M., Ortiz, J.E., Sánchez-Palencia, Y., Caldara, M., 2021. Refining the middle-late Pleistocene chronology of marine terraces and uplift history in a sector of the Apulian foreland (southern Italy) by applying a synchronous correlation technique and amino acid racemization to Patella spp. and Thetystrombus latus. Italian Journal of Geosciences 140 (3), 438–463.
De Santis, V., Scardino, G., Scicchitano, G., Meschis, M., Montagna, P., Pons-Branchu, E., et al., 2023. Middle-late Pleistocene chronology of palaeoshorelines and uplift history in the low-rising to stable Apulian foreland: overprinting and reoccupation. Geomorphology 421, 108530.
Devescovi, M., Iveša, L., 2008. Colonization patterns of the date mussel Lithophaga lithophaga (L., 1758) on limestone breakwater boulders of a marina. Period. Biol. 110 (4), 339–345.
Dunai, T.J., 2010. Cosmogenic Nuclides: Principles, Concepts and Applications in the Earth Surface Sciences. Cambridge University Press.
EMERGEO Working Group, 2010. Evidence for surface rupture associated with the Mw 6.3 L'Aquila earthquake sequence of April 2009 (central Italy). Terra. Nova 22 (1), 43–51.

Fassoulas, C., Kilias, A., Mountrakis, D., 1994. Postnappe stacking extension and exhumation of high-pressure/low-temperature rocks in the island of Crete, Greece. Tectonics 13 (1), 127–138.

Ferranti, L., Antonioli, F., Mauz, B., Amorosi, A., Dai Pra, G., Mastronuzzi, G., et al., 2006. Markers of the last interglacial sea-level high stand along the coast of Italy: tectonic implications. Quat. Int. 145, 30–54.

Ferranti, L., Burrato, P., Sechi, D., Andreucci, S., Pepe, F., Pascucci, V., 2021. Late Quaternary coastal uplift of southwestern Sicily, central Mediterranean sea. Quat. Sci. Rev. 255, 106812.

Fossen, H., Rotevatn, A., 2016. Fault linkage and relay structures in extensional settings—a review. Earth Sci. Rev. 154, 14–28.

Gaki-Papanastassiou, K., Karymbalis, E., Papanastassiou, D., Maroukian, H., 2009. Quaternary marine terraces as indicators of neotectonic activity of the Ierapetra normal fault SE Crete (Greece). Geomorphology 104 (1–2), 38–46.

Gallen, S.F., Wegmann, K.W., Bohnenstiehl, D.R., Pazzaglia, F.J., Brandon, M.T., Fassoulas, C., 2014. Active simultaneous uplift and margin-normal extension in a forearc high, Crete, Greece. Earth Planet Sci. Lett. 398, 11–24.

Ganas, A., Parsons, T., 2009. Three-dimensional model of Hellenic Arc deformation and origin of the Cretan uplift. J. Geophys. Res. Solid Earth 114 (B6).

Ganas, A., Oikonomou, I.A., Tsimi, C., 2013. NOAfaults: a digital database for active faults in Greece. Bull. Geol. Soc. Greece 47 (2), 518–530. https://doi.org/10.12681/bgsg.11079.

Ganas, A., Elias, P., Briole, P., Valkaniotis, S., Escartin, J., Tsironi, V., Karasante, I, Kosma, Chr., 2021. Co-seismic and post-seismic deformation, field observations and fault model of the 30 October 2020 Mw = 7.0 Samos earthquake, Aegean Sea. Acta Geophys. 69, 999–1024. https://doi.org/10.1007/s11600-021-00599-1.

Ganas, A., Fassoulas, C., Moshou, A., Bozionelos, G., Papathanassiou, G., Tsimi, C., Valkaniotis, S., 2017. Geological and seismological evidence for NW-SE crustal extension at the southern margin of Heraklion basin, Crete. Bull. Geol. Soc. Greece 51, 52–75.

Ganas, A., Tsironi, V., Kollia, E., Delagas, M., Tsimi, C., Oikonomou, A., 2018. Recent Upgrades of the NOA Database of Active Faults in Greece (NOAFAULTs). Proceedings of the 19th General Assembly of WEGENER, Grenoble, France, pp. 10–13.

Ganas, A., Hamiel, Y., Serpetsidaki, A., Briole, P., Valkaniotis, S., Fassoulas, C., et al., 2022. The arkalochori Mw= 5.9 earthquake of 27 september 2021 inside the heraklion basin: a shallow, blind rupture event highlighting the orthogonal extension of central Crete. Geosciences 12 (6), 220.

Gosse, J.C., Phillips, F.M., 2001. Terrestrial in situ cosmogenic nuclides: theory and application. Quat. Sci. Rev. 20 (14), 1475–1560.

Gowan, E.J., Zhang, X., Khosravi, S., Rovere, A., Stocchi, P., Hughes, A.L., et al., 2021. A new global ice sheet reconstruction for the past 80 000 years. Nat. Commun. 12 (1), 1199.

Heisinger, B., Lal, D., Jull, A.J.T., Kubik, P., Ivy-Ochs, S., Knie, K., Nolte, E., 2002a. Production of selected cosmogenic radionuclides by muons: 2. Capture of negative muons. Earth Planet Sci. Lett. 200 (3–4), 357–369.

Heisinger, B., Lal, D., Jull, A.J.T., Kubik, P., Ivy-Ochs, S., Neumaier, S., et al., 2002b. Production of selected cosmogenic radionuclides by muons: 1. Fast muons. Earth Planet Sci. Lett. 200 (3–4), 345–355.

Houghton, S.L., Roberts, G.P., Papanikolaou, I.D., McArthur, J.M., Gilmour, M.A., 2003. New 234U-230Th coral dates from the western Gulf of Corinth: implications for extensional tectonics. Geophys. Res. Lett. 30 (19).

Howell, A., Jackson, J., Copley, A., McKenzie, D., Nissen, E., 2017. Subduction and vertical coastal motions in the eastern Mediterranean. Geophys. J. Int. 211 (1), 593–620.

Imanishi, K., Ando, R., Kuwahara, Y., 2012. Unusual shallow normal-faulting earthquake sequence in compressional northeast Japan activated after the 2011 off the Pacific coast of Tohoku earthquake. Geophys. Res. Lett. 39 (9).

Institute for Geology and Mineral Exploration (IGME), 1969. Geological map of Greece. Alikianou Sheet 1 (50), 000.

Institute for Geology and Mineral Exploration (IGME), 1995. Geological map of Greece. Paleochora Sheet 1 (50), 000.

Jackson, J., 1994. Active tectonics of the Aegean region. Annual Rev. Earth Planet. Sci. 22 (1), 239–271.

Jara-Munoz, J., Melnick, D., Brill, D., Strecker, M.R., 2015. Segmentation of the 2010 Maule Chile earthquake rupture from a joint analysis of uplifted marine terraces and seismic-cycle deformation patterns. Quat. Sci. Rev. 113, 171–192.

Jara-Muñoz, J., Melnick, D., Zambrano, P., Rietbrock, A., González, J., Argandoña, B., Strecker, M.R., 2017. Quantifying offshore fore-arc deformation and splay-fault slip using drowned Pleistocene shorelines, Arauco Bay, Chile. J. Geophys. Res. Solid Earth 122 (6), 4529–4558.

Kiratzi, A., Louvari, E., 2003. Focal mechanisms of shallow earthquakes in the Aegean Sea and the surrounding lands determined by waveform modelling: a new database. J. Geodyn. 36 (1–2), 251–274.

Kokinou, E., Tiago, A., Evangelos, K., 2012. Structural decoupling in a convergent forearc setting (southern Crete, Eastern Mediterranean). Bulletin 124 (7–8), 1352–1364.

Kreemer, C., Chamot-Rooke, N., 2004. Contemporary kinematics of the southern aegean and the mediterranean ridge. Geophys. J. Int. 157 (3), 1377–1392.

Laborel, J., 1986. Vermetid gastropods as sea-level indicators. Sea-level research: a manual for the collection and evaluation of data 281–310.

Laborel, J., Laborel-Deguen, F., 1994. Biological indicators of relative sea-level variations and of co-seismic displacements in the Mediterranean region. J. Coast Res. 395–415.

Lajoie, K.R., 1986. Coastal tectonics. Active tectonics 95–124.

Lambeck, K., Chappell, J., 2001. Sea level change through the last glacial cycle. Science 292 (5517), 679–686.

Licciardi, J.M., Denoncourt, C.L., Finkel, R.C., 2008. Cosmogenic 36Cl production rates from Ca spallation in Iceland. Earth Planet Sci. Lett. 267 (1–2), 365–377.

Litchfield, N.J., Clark, K.J., Cochran, U.A., Palmer, A.S., Mountjoy, J., Mueller, C., et al., 2020. Marine terraces reveal complex near-shore upper-plate faulting in the northern hikurangi margin, new ZealandMarine terraces reveal complex near-shore upper-plate faulting in the northern hikurangi margin, New Zealand. Bull. Seismol. Soc. Am. 110 (2), 825–849.

Marrero, S.M., Phillips, F.M., Borchers, B., Lifton, N., Aumer, R., Balco, G., 2016a. Cosmogenic nuclide systematics and the CRONUScalc program. Quat. Geochronol. 31, 160–187.

Marrero, S.M., Phillips, F.M., Caffee, M.W., Gosse, J.C., 2016b. CRONUS-Earth cosmogenic 36Cl calibration. Quat. Geochronol. 31, 199–219.

Mascle, J., Le Quellec, P., Leité, O., Jongsma, D., 1982. Structural sketch of the Hellenic continental margin between the western Peloponnesus and eastern Crete. Geology 10 (2), 113–116.

Matsu'ura, T., Kimura, H., Komatsubara, J., Goto, N., Yanagida, M., Ichikawa, K., Furusawa, A., 2014. Late Quaternary uplift rate inferred from marine terraces, Shimokita Peninsula, northeastern Japan: a preliminary investigation of the buried shoreline angle. Geomorphology 209, 1–17.

Matsu'ura, T., 2015. Late Quaternary uplift rate inferred from marine terraces, Muroto Peninsula, southwest Japan: forearc deformation in an oblique subduction zone. Geomorphology 234, 133–150.

Mechernich, S., Reicherter, K., Deligiannakis, G., Papanikolaou, I., 2022. Tectonic geomorphology of active faults in Eastern Crete (Greece) with slip rates and earthquake history from cosmogenic 36Cl dating of the Lastros and Orno faults. Quat. Int.

Meier, T., Rische, M., Endrun, B., Vafidis, A., Harjes, H.P., 2004. Seismicity of the Hellenic subduction zone in the area of western and central Crete observed by temporary local seismic networks. Tectonophysics 383 (3–4), 149–169.

Menant, A., Angiboust, S., Gerya, T., Lacassin, R., Simoes, M., Grandin, R., 2020. Transient stripping of subducting slabs controls periodic forearc uplift. Nat. Commun. 11 (1), 1823.

Mercier, J.L., Sorel, D., Vergely, P., Simeakis, K., 1989. Extensional tectonic regimes in the Aegean basins during the Cenozoic. Basin Res. 2 (1), 49–71.

Meschis, M., Roberts, G.P., Robertson, J., Briant, R.M., 2018. The relationships between regional quaternary uplift, deformation across active normal faults, and historical seismicity in the upper plate of Subduction zones: the Capo D'Orlando fault, NE Sicily. Tectonics 37 (5), 1231–1255.

Meschis, M., Roberts, G.P., Robertson, J., Mildon, Z.K., Sahy, D., Goswami, R., et al., 2022. Out of phase Quaternary uplift-rate changes reveal normal fault interaction, implied by deformed marine palaeoshorelines. Geomorphology 416, 108432.

Mildon, Z.K., Toda, S., Faure Walker, J.P., Roberts, G.P., 2016. Evaluating models of Coulomb stress transfer: is variable fault geometry important? Geophys. Res. Lett. 43 (24), 12–407.

Miller, W.R., Mason, T.R., 1994. Erosional features of coastal beachrock and aeolianite outcrops in Natal and Zululand, South Africa. J. Coast Res. 374–394.

Mouslopoulou, V., Begg, J., Nicol, A., Oncken, O., Prior, C., 2015a. Formation of late quaternary paleoshorelines in Crete, eastern mediterranean. Earth Planet Sci. Lett. 431, 294–307.

Mouslopoulou, V., Nicol, A., Begg, J., Oncken, O., Moreno, M., 2015b. Clusters of megaearthquakes on upper plate faults control the Eastern Mediterranean hazard. Geophys. Res. Lett. 42 (23), 10–282.

Muhs, D.R., Rockwell, T.K., Kennedy, G.L., 1992. Late Quaternary uplift rates of marine terraces on the Pacific coast of North America, southern Oregon to Baja California Sur. Quat. Int. 15, 121–133.

Muhs, D.R., Kennedy, G.L., Rockwell, T.K., 1994. Uranium-series ages of marine terrace corals from the Pacific coast of North America and implications for last-interglacial sea level history. Quat. Res. 42 (1), 72–87.

Nicol, A., Mouslopoulou, V., Begg, J., Oncken, O., 2020. Displacement accumulation and sampling of paleoearthquakes on active normal faults of Crete in the eastern Mediterranean. G-cubed 21 (11), e2020GC009265.

Nocquet, J.M., 2012. Present-day kinematics of the Mediterranean: a comprehensive overview of GPS results. Tectonophysics 579, 220–242.

Normand, R., Simpson, G., Herman, F., Biswas, R.H., Bahroudi, A., Schneider, B., 2019. Dating and morpho-stratigraphy of uplifted marine terraces in the Makran subduction zone (Iran). Earth Surf. Dyn. 7 (1), 321–344.

Ortlieb, L., Zazo, C., Goy, J., Hillaire-Marcel, C., Ghaleb, B., Cournoyer, L., 1996. Coastal deformation and sea-level changes in the northern Chile subduction area (23 S) during the last 330 ky. Quat. Sci. Rev. 15 (8–9), 819–831.

Ott, R.F., Gallen, S.F., Wegmann, K.W., Biswas, R.H., Herman, F., Willett, S.D., 2019. Pleistocene terrace formation, Quaternary rock uplift rates and geodynamics of the Hellenic Subduction Zone revealed from dating of paleoshorelines on Crete, Greece. Earth Planet Sci. Lett. 525, 115757.

Ott, R.F., Wegmann, K.W., Gallen, S.F., Pazzaglia, F.J., Brandon, M.T., Ueda, K., Fassoulas, C., 2021. Reassessing Eastern Mediterranean tectonics and earthquake hazard from the 365 CE earthquake. AGU Advances 2 (2), e2020AV000315.

Ott, R.F., Scherler, D., Wegmann, K.W., D'Arcy, M.K., Pope, R.J., Ivy-Ochs, S., et al., 2023. Paleo-denudation rates suggest variations in runoff drove aggradation during last glacial cycle, Crete, Greece. Earth Surf. Process. Landforms 48 (2), 386–405.

Papadimitriou, E.E., Karakostas, V.G., 2008. Rupture model of the great AD 365 Crete earthquake in the southwestern part of the Hellenic Arc. Acta Geophys. 56 (2), 293.

Papadopoulos, G., 2011. A seismic history of Crete 65 (66), 385.

Papanikolaou, D., Vassilakis, E., 2010. Thrust faults and extensional detachment faults in Cretan tectono-stratigraphy: implications for Middle Miocene extension. Tectonophysics 488 (1–4), 233–247.

Papazachos, B.C., 1990. Seismicity of the Aegean and surrounding area. Tectonophysics 178 (2–4), 287–308.

Papazachos, B.C., Karakostas, V.G., Papazachos, C.B., Scordilis, E.M., 2000. The geometry of the Wadati–Benioff zone and lithospheric kinematics in the Hellenic arc. Tectonophysics 319 (4), 275–300.

Pedoja, K., Jara-Muñoz, J., De Gelder, G., Robertson, J., Meschis, M., Fernández-Blanco, D., et al., 2018. Neogene-Quaternary slow coastal uplift of Western Europe through the perspective of sequences of strandlines from the Cotentin Peninsula (Normandy, France). Geomorphology 303, 338–356.

Phillips, F.M., Stone, W.D., Fabryka-Martin, J.T., 2001. An improved approach to calculating low-energy cosmic-ray neutron fluxes near the land/atmosphere interface. Chem. Geol. 175 (3–4), 689–701.

Pirazzoli, P.A., Thommeret, J., Thommeret, Y., Laborel, J., Montag-Gioni, L.F., 1982. Crustal block movements from Holocene shorelines: Crete and antikythira (Greece). Tectonophysics 86 (1–3), 27–43.

Pirazzoli, P.A., 1986. Marine notches. Sea-level research: a manual for the collection and evaluation of data 361–400.

Pirazzoli, P.A., Laborel, J., Stiros, S.C., 1996. Earthquake clustering in the Eastern Mediterranean during historical times. J. Geophys. Res. Solid Earth 101 (B3), 6083–6097.

Pirazzoli, P.A., 2005. A review of possible eustatic, isostatic and tectonic contributions in eight late-Holocene relative sea-level histories from the Mediterranean area. Quat. Sci. Rev. 24 (18–19), 1989–2001.

Roberts, G.P., Houghton, S.L., Underwood, C., Papanikolaou, I., Cowie, P.A., van Calsteren, P., et al., 2009. Localization of Quaternary slip rates in an active rift in 105 years: an example from central Greece constrained by 234U-230Th coral dates from uplifted paleoshorelines. J. Geophys. Res. Solid Earth 114 (B10).

Roberts, G.P., Meschis, M., Houghton, S., Underwood, C., Briant, R.M., 2013. The implications of revised Quaternary palaeoshoreline chronologies for the rates of active extension and uplift in the upper plate of subduction zones. Quat. Sci. Rev. 78, 169–187.

Robertson, J., Meschis, M., Roberts, G.P., Ganas, A., Gheorghiu, D.M., 2019. Temporally constant Quaternary uplift rates and their relationship with extensional upper-plate faults in south Crete (Greece), constrained with 36Cl cosmogenic exposure dating. Tectonics 38 (4), 1189–1222.

Robertson, J., Roberts, G.P., Iezzi, F., Meschis, M., Gheorghiu, D.M., Sahy, D., et al., 2020. Distributed normal faulting in the tip zone of the South Alkyonides Fault System, Gulf of Corinth, constrained using 36Cl exposure dating of late-Quaternary wave-cut platforms. J. Struct. Geol. 136, 104063.

Rohling, E.J., Foster, G.L., Grant, K.M., Marino, G., Roberts, A.P., Tamisiea, M.E., Williams, F., 2014. Sea-level and deep-sea-temperature variability over the past 5.3 million years. Nature 508 (7497), 477–482.

Rovere, A., Raymo, M.E., Vacchi, M., Lorscheid, T., Stocchi, P., Gomez-Pujol, L., et al., 2016. The analysis of Last Interglacial (MIS 5e) relative sea-level indicators: reconstructing sea-level in a warmer world. Earth Sci. Rev. 159, 404–427.

Sachpazi, M., Kapetanidis, V., Charalampakis, M., Laigle, M., Kissling, E., Fokaefs, A., et al., 2020. Methoni Mw 6.8 rupture and aftershocks distribution from a dense array of OBS and land seismometers, offshore SW Hellenic subduction. Tectonophysics 796, 228643.

Saillard, M., Hall, S.R., Audin, L., Farber, D.L., Hérail, G., Martinod, J., et al., 2009. Non-steady long-term uplift rates and Pleistocene marine terrace development along the Andean margin of Chile (31 S) inferred from 10Be dating. Earth Planet Sci. Lett. 277 (1–2), 50–63.

Saillard, M., Hall, S.R., Audin, L., Farber, D.L., Regard, V., Hérail, G., 2011. Andean coastal uplift and active tectonics in southern Peru: 10Be surface exposure dating of differentially uplifted marine terrace sequences (San Juan de Marcona,~ 15.4 S). Geomorphology 128 (3–4), 178–190.

Sakellariou, D., Tsampouraki-Kraounaki, K., 2019. Plio-Quaternary extension and strike-slip tectonics in the Aegean. In: Transform Plate Boundaries and Fracture Zones. Elsevier, pp. 339–374.

Schimmelpfennig, I., Benedetti, L., Finkel, R., Pik, R., Blard, P.H., Bourlès, D., et al., 2009. Sources of in-situ 36Cl in basaltic rocks. Implications for calibration of production rates. Quat. Geochronol. 4 (6), 441–461.

Schlagenhauf, A., Gaudemer, Y., Benedetti, L., Manighetti, I., Palumbo, L., Schimmelpfennig, I., et al., 2010. Using in situ Chlorine-36 cosmonuclide to recover past earthquake histories on limestone normal fault scarps: a reappraisal of methodology and interpretations. Geophys. J. Int. 182 (1), 36–72.

Shakun, J.D., Lea, D.W., Lisiecki, L.E., Raymo, M.E., 2015. An 800-kyr record of global surface ocean δ18O and implications for ice volume-temperature coupling. Earth Planet Sci. Lett. 426, 58–68.

Shaw, B., Ambraseys, N.N., England, P.C., Floyd, M.A., Gorman, G.J., Higham, T.F.G., et al., 2008. Eastern Mediterranean tectonics and tsunami hazard inferred from the AD 365 earthquake. Nat. Geosci. 1 (4), 268–276.

Shaw, B., Jackson, J.A., Higham, T.F.G., England, P.C., Thomas, A.L., 2010. Radiometric dates of uplifted marine fauna in Greece: implications for the interpretation of recent earthquake and tectonic histories using lithophagid dates. Earth Planet Sci. Lett. 297 (3–4), 395–404.

Siddall, M., Rohling, E.J., Almogi-Labin, A., Hemleben, C., Meischner, D., Schmelzer, I., Smeed, D.A., 2003. Sea-level fluctuations during the last glacial cycle. Nature 423 (6942), 853–858.

Skourtsos, E., Pope, R., Triantaphylleou, M.V., 2007. Tectono-sedimentary evolution and rates of tectonic uplift of the Sfakia coastal zone, southwestern Crete. Bull. Geol. Soc. Greece: Proceedings of the 11th International Congress 40 (1), 475–487.

Spratt, R.M., Lisiecki, L.E., 2016. A Late Pleistocene sea level stack. Clim. Past 12 (4), 1079–1092.

Stephenson, T.A., Stephenson, A., 1949. The universal features of zonation between tide-marks on rocky coasts. J. Ecol. 289–305.

Stiros, S.C., 1996. Late Holocene relative sea level changes in SW Crete: evidence of an unusual earthquake cycle. Ann. Geofisc. 39 (3).

Stiros, S.C., 2001. The AD 365 Crete earthquake and possible seismic clustering during the fourth to sixth centuries AD in the Eastern Mediterranean: a review of historical and archaeological data. J. Struct. Geol. 23 (2–3), 545–562.

Stiros, S., Drakos, A., 2006. A fault-model for the tsunami-associated, magnitude≥ 8.5 Eastern Mediterranean, AD365 earthquake. Z. Geomorphol. 146, 125–137.

Stiros, S.C., 2010. The 8.5+ magnitude, AD365 earthquake in Crete: coastal uplift, topography changes, archaeological and historical signature. Quat. Int. 216 (1–2), 54–63.

Stone, J., Lambeck, K., Fifield, L.K., Evans, J.T., Cresswell, R.G., 1996. A lateglacial age for the main rock platform, western Scotland. Geology 24 (8), 707–710.

Strasser, T.F., Runnels, C., Wegmann, K., Panagopoulou, E., Mccoy, F., Digregorio, C., et al., 2011. Dating palaeolithic sites in southwestern Crete, Greece. J. Quat. Sci. 26 (5), 553–560.

Taymaz, T., Jackson, J., Westaway, R., 1990. Earthquake mechanisms in the hellenic trench near Crete. Geophys. J. Int. 102 (3), 695–731.

Ten Veen, J.H., Meijer, P.T., 1998. Late Miocene to Recent tectonic evolution of Crete (Greece): geological observations and model analysis. Tectonophysics 298 (1–3), 191–208.

Ten Veen, J.H., Kleinspehn, K.L., 2003. Incipient continental collision and plate-boundary curvature: late Pliocene–Holocene transtensional Hellenic forearc, Crete, Greece. J. Geol. Soc. 160 (2), 161–181.

Tiberti, M.M., Basili, R., Vannoli, P., 2014. Ups and downs in western Crete (Hellenic subduction zone). Sci. Rep. 4 (1), 5677.

Toda, S., Stein, R.S., Sevilgen, V., Lin, J., 2011. Coulomb 3.3 Graphic-rich deformation and stress-change software for earthquake, tectonic, and volcano research and teaching—user guide. US Geological Survey open-file report 1060, 63, 2011.

Toda, S., Tsutsumi, H., 2013. Simultaneous reactivation of two, subparallel, inland normal faults during the M w 6.6 11 April 2011 Iwaki earthquake triggered by the M w 9.0 Tohoku-oki, Japan, earthquake. Bull. Seismol. Soc. Am. 103 (2B), 1584–1602.

Tsimi, C., Ganas, A., Ferrier, G., Drakatos, G., Pope, R.J., Fassoulas, C., 2007. October). Morphotectonics of the Sfakia normal fault, southwestern Crete, Greece. In: Proceedings of 8th Pan-Hellenic Geographical Conference, pp. 4–7.

Trenhaile, A.S., 2000. Modeling the development of wave-cut shore platforms. Mar. Geol. 166 (1–4), 163–178.

Vittori, E., Di Manna, P., Blumetti, A.M., Comerci, V., Guerrieri, L., Esposito, E., et al., 2011. Surface faulting of the 6 April 2009 M w 6.3 L'Aquila earthquake in central Italy. Bull. Seismol. Soc. Am. 101 (4), 1507–1530.

Waelbroeck, C., Labeyrie, L., Michel, E., Duplessy, J.C., Mcmanus, J.F., Lambeck, K., et al., 2002. Sea-level and deep water temperature changes derived from benthic foraminifera isotopic records. Quat. Sci. Rev. 21 (1–3), 295–305.

Walters, R.J., Elliott, J.R., D'Agostino, N., England, P.C., Hunstad, I., Jackson, J.A., et al., 2009. The 2009 L'Aquila earthquake (central Italy): a source mechanism and implications for seismic hazard. Geophys. Res. Lett. 36 (17).

Wegmann, K.W., 2008. Tectonic Geomorphology above Mediterranean Subduction Zones: Northeastern Apennines of Italy and Crete, Greece. Lehigh University, Proquest [Doctoral thesis]. https://www.proquest.com/openview/b4a7fbc5b8f0fffc3ae42219f5f86506/1?pq-origsite=gscholar&cbl=18750.

Wells, D.L., Coppersmith, K.J., 1994. New empirical relationships among magnitude, rupture length, rupture width, rupture area, and surface displacement. Bull. Seismol. Soc. Am. 84 (4), 974–1002.

Westaway, R., 1993. Quaternary uplift of southern Italy. J. Geophys. Res. Solid Earth 98 (B12), 21741–21772.

Wilkinson, M., Roberts, G.P., McCaffrey, K., Cowie, P.A., Walker, J.P.F., Papanikolaou, I., et al., 2015. Slip distributions on active normal faults measured from LiDAR and field mapping of geomorphic offsets: an example from L'Aquila, Italy, and implications for modelling seismic moment release. Geomorphology 237, 130–141.

Yolsal-Çevikbilen, S., Taymaz, T., 2012. Earthquake source parameters along the Hellenic subduction zone and numerical simulations of historical tsunamis in the Eastern Mediterranean. Tectonophysics 536, 61–100.

Zygouri, V., Koukouvelas, I., Ganas, A., 2016. Palaeoseismological analysis of the east giouchtas fault, heraklion basin, Crete (preliminary results). Bull. Geol. Soc. Greece 50 (1), 563–571.